

Ripening of one-dimensional molecular nanostructures on insulating surfaces

Master Thesis

Tobias Richter

Fachgebiet Theoretische Physik II
Institut für Physik
Fakultät für Mathematik und Naturwissenschaften
TU Ilmenau

July 8, 2011

Contents

1	Introduction	4
2	Nucleation, growth and ripening	6
2.1	Fundamental processes in nanostructure formation	6
2.2	Submonolayer growth during epitaxy	7
2.3	Ripening	11
3	Growth of helicenes on calcite (104) surfaces	13
3.1	Experimental Setup	13
3.2	Experimental findings	15
4	Growth modeling	19
4.1	Basis model	19
4.2	Edge diffusion (ED)	20
4.2.1	Standard edge diffusion mechanism	22
4.2.2	Instantaneous edge diffusion	22
4.2.3	Edge diffusion limited by maximum distance	23
4.3	Dimerization	24
4.4	Model I: Monomers (M)	26
4.5	Model II: Monomers and instantaneous edge diffusion (MIE)	26
4.6	Model III: Monomers and edge diffusion limited by maximum distance (MLE)	26
4.7	Model IV: Including dimer structures (D)	26
4.8	Model V: Dimers and conventional edge diffusion (DCE)	26
4.9	Model VI: Dimers and instantaneous edge diffusion (DIE)	26
4.10	Model VII: Dimers and edge diffusion limited by maximum distance (DLE)	27
4.11	Model parameters	27
5	Results of growth simulations	29
5.1	Model I	29
5.2	Model II	31
5.3	Model III	33
5.4	Model IV	38
5.5	Model V	41
5.6	Model VI	43
5.7	Model VII	46
5.8	Model comparison	48
6	Summary and Outlook	56
7	Appendix	59
7.1	KMC	59
7.2	References	63

7.3	Erklärung	68
7.4	Acknowledgements	69

1 Introduction

The search of new concepts for building electronic devices goes along with the technological challenge to achieve significantly lower electronic device sizes down to the atomic scale, because of the well-known physical limits in silicon technology. To overcome obstacles of silicon-based electronic devices, promising material systems are electrical devices based on organic building blocks. Current research is concerned with the development of molecular transistors and nanowires [1, 2, 3, 4, 5]. It is thus desirable to search for organic materials leading to one-dimensional wires, which are, however, fabricated on nonconducting (insulating) rather than conducting (metallic) substrates. In this connection self-assembly became of great importance to enable the tailoring of such molecular structures (for review see [6]). Grown structures on insulating substrates can be studied by means of non-contact atomic force microscopy (NC-AFM). Questions arise about the understanding of the basic mechanisms behind molecular self-assembly. Subsequently, in order to produce wire-like structures in a predictable manner, it is crucial to illuminate the underlying main processes and their interplay during the growth and ripening in the deposition and post-deposition regime, respectively.

In search of suitable material systems that utilize molecular self-assembly for creating one-dimensional molecular structures on insulating surfaces the group of A. Kühnle at the University of Mainz [7] found that a derivative of helicene exhibits growth of wire-like structures on a calcite (104) surface, which has large, nearly defect-free terraces. These structures were produced experimentally by sublimating organic molecules on this insulating surface. The wire-like structures formed by the helicenes are on flat terraces and are of well-defined width. All self-assembled one-dimensional rows are directed along the [010] direction of the calcite surface. Later stage AFM observations of these wire-like structures in the post-deposition regime reveal two coarsening regimes. At the beginning the mean length increases rapidly and grows linear in time, while their number decreases, but the volume fraction of the wires remains constant. As time proceeds, a crossover to a regime, where the mean length of wire-like helicenes remains nearly constant, can be observed.

This thesis focuses on the investigation and understanding of the growth and ripening kinetics of helicene nanostructures on calcite substrates. Despite the rather shallow number of degrees of freedom in such systems, the kinetics can be very complex and are in general not describable by analytical expressions in a satisfactory way. To this end continuous-time kinetic Monte Carlo simulations are performed for models of varying complexity in order to identify the underlying processes responsible for the experimentally observed ripening kinetics of wire-like helicene structures in the post-deposition regime.

The structure of this work is as follows: Chapter 2 introduces basic processes, quantities and concepts of nanostructure formation on clean surfaces within the deposition regime and post-deposition regime. In Chapter 3 the helicene growth experiments on calcite

(104) surfaces are explained. This chapter concludes with a survey of the experimental observations of helicene structure formation in the post-deposition regime. In Chapter 4 we develop models with increasing complexity in order to illuminate the main processes behind the observed coarsening (ripening) of wire-like helicene structures on insulating surfaces after deposition. Chapter 5 presents continuous-time Monte Carlo simulation studies of the model variants explained in chapter 4, concluding with a discussion of the results. This thesis concludes with Chapter 6 which contains a summary of main results and their successful explanations of the experimental findings.

2 Nucleation, growth and ripening

This chapter is concerned with the basic processes, quantities and concepts of nanostructure formation on clean surfaces within the deposition regime and post-deposition regime, respectively. The main atomistic processes, which are relevant during the self-organized growth of nanoclusters, are introduced in the first section. The second section reviews mean-field rate equation theories, which are successfully in explaining important aspects of the growth kinetics during submonolayer deposition. Hence most of these nanostructures are produced by means of Molecular Beam Epitaxy (MBA) or vapor deposition. This chapter concludes with a typical mechanism, which is important for explaining how nanostructures develop after deposition.

2.1 Fundamental processes in nanostructure formation

On microscopic scales, structures evolve by atomic moves that obey fairly simple rules. Figure 2.1 illustrates the main elementary moves, which dominate the early stage of growth in Epitaxy. Due to the interplay of various processes, such as adatom deposition, diffusion, nucleation, aggregation, detachment, evaporation, coalescence, a stochastic description is appropriate to describe nanoscopic structures.

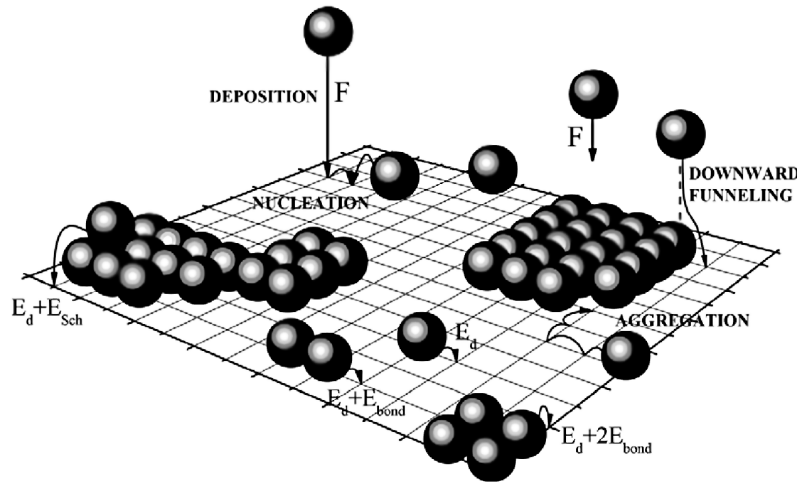


Figure 2.1: Illustration of the main processes during early Epitaxy. Taken from [8].

The initial growth starts with the deposition of monomers or molecules determined by the incoming flux F on a clean two-dimensional surface which are flat down to the atomic scale. At sufficiently high temperatures, the adatoms can reevaporate. In a wide temperature range typically for a plenty of experiments this reevaporation can be neglected and the adatoms stick to the surface. Note that it is also possible for the deposited particles to be chemisorbed at the surface, i.e., a chemical bond is formed with other surface atoms or molecules, but this does not occur in the systems studied in this thesis.

After the molecules land on the substrate, adatoms perform most of their time a vibrational motion around their lattice position before they hop thermally activated to neighboring free lattice sites. Based on transition state theory [9] the thermal activated jump processes occur with a jump rate

$$\nu = \nu_0 e^{-\frac{E_D}{k_B T}}, \quad (2.1)$$

where E_D is the diffusion barrier at temperature T , k_B is the Boltzmann constant, and ν_0 the attempt frequency. The prefactor ν_0 lies typically in the range between $10^{11} \frac{1}{s}$ and $10^{13} \frac{1}{s}$ [10]. A sequence of a large number of adatom hopping moves leads to a two-dimensional random walk on the substrate. Thus, the mean square displacement of the position $\vec{r}(t)$ increases linear in time according to

$$\langle (\vec{r}(t) - \vec{r}(0))^2 \rangle = \nu a^2 t = 4Dt, \quad (2.2)$$

where a is the distance between two adjacent lattice sites and D is the diffusion coefficient. If diffusing adatoms meet each other they can form two-dimensional critical nuclei of size $s = i^*$, which can either dissociate by detachment processes or can grow to clusters and islands by attachment of further adatoms. Nucleation and growth are competing processes. Note that the concept of the critical nucleus is a dynamical one, where i^* may be changed by varying the temperature [11]. Moreover, i^* also depends on the lattice geometry [8, 12]. At very low temperature, already two adatoms form a stable dimer ($i^* = 1$). This regime is well investigated and known as diffusion limited aggregation [10]. This growth mode is often called hit and stick leading to fractal islands. With increasing temperatures double bounded atoms become stable, which implies $i^* = 2$ for the minimal stable structure on triangular lattices (triangles formed by three adatoms are stable) and $i^* = 3$ for square lattices (the minimal stable structure is a square formed by four adatoms), respectively. Another important process regarding the formation of structures in thin film growth is edge diffusion. Edge diffusion is among others responsible for the relaxation of island shapes [8, 13]. For example the onset of edge diffusion at elevated temperatures leads to a transition from fractal islands to more compact ones [13] and is also crucial for the formation of square shaped islands [8].

2.2 Submonolayer growth during epitaxy

In this section some general aspects about growth during early stage deposition will be reviewed. An important quantity in the submonolayer growth regime is the number density of islands N before the substrate is completely covered, which allows one to determine key parameters of the growth kinetics, such as activation energies and sizes i^* of critical nuclei as function of the temperature. The understanding of the initial submonolayer regime helps to control the formation of self-organized nanostructures and thin film devices at later stages.

The first stage in surface growth proceeds by the assembly of two-dimensional islands composed of adsorbate atoms on the substrate. The growth kinetics in this stage are mainly affected by the ratio of timescales for diffusion and deposition, i.e.,

$$\Gamma = \frac{D}{F}. \quad (2.3)$$

For typical experimental situations the relevant range of Γ lies between $10^5 < \Gamma < 10^{11}$. It should be noted that such Γ values imply that the growth during submonolayer epitaxy takes places far from equilibrium and thermodynamic approaches are insufficient for describing the emerging structures and quantities (for review see [10], and references therein). For deposition of one type of atom, important aspects of the growth kinetics in the submonolayer regime were successfully described by the mean-field rate equation (MFRE) theory pioneered by Venables and co-worker [14, 15, 16]. This kinetic approach is based on a coupled set of balance equations, which specify the time evolution of the adatom density n_1 and islands n_s of size s . Mostly adatoms are the only mobile species, that means clusters with more than two adatoms can be considered as immobile species. Moreover, we assume that atom movements between the first and second layer can be disregarded at low coverages. The MFRE for such a situation at low temperatures (no re-evaporation) are

$$\frac{dn_1}{dt} = F - 2D\sigma_1 n_1^2 - \sum_{s>1} Dn_1\sigma_s n_s + \sum_{1<s\leq i^*} k_s n_s \quad (2.4)$$

$$\frac{dn_s}{dt} = Dn_1(\sigma_{s-1}n_{s-1} - \sigma_s n_s) - k_s n_s + k_{s+1}n_{s+1}. \quad (2.5)$$

These equations refer to the growth regime, where coalescence events of islands should be negligible. As mentioned in Sec. 2.1 the incoming flux is F and D is the diffusion coefficient. In Eqs. (2.4) and (2.5) the attachment of diffusing adatoms to s -cluster occurs with rates $\sigma_s Dn_1 n_s$, where σ_s are the capture numbers. The dissociation of clusters of size s occurs with rates k_s (i.e. the detachment of monomers). By introducing a critical nucleus of size i^* (see also Sec. 2.1), clusters with $s > i^*$ are stable and we can set $k_s = 0$ for $s > i^*$ in Eqs. (2.4) and (2.5). Clusters of size $2 \leq s \leq i^*$ are unstable. Assuming that for unstable clusters the attachment and decay processes satisfy a detailed balance relation, i.e., $k_s n_s \simeq D\sigma_{s-1} n_1 n_{s-1}$, the Walton relations follow [10, 14, 17]

$$n_s \simeq n_1^s e^{E_s/k_B T}; \quad 2 \leq s \leq i^*, \quad (2.6)$$

where $E_s > 0$ is the binding energy of a s -cluster. Introducing the total number density of stable islands

$$N = \sum_{s>i^*} n_s \quad (2.7)$$

and the average capture number

$$\bar{\sigma} = \frac{1}{N} \sum_{s=i^*+1}^{\infty} \sigma_s n_s, \quad (2.8)$$

a reduced set of equations for $n_1(t)$ and $N(t)$ can be derived from Eqs. (2.4) and (2.5). Using the steady state condition $n_1 \approx \frac{F}{D\bar{\sigma}N}$, whose solution predicts the following scaling relation for number density of stable [10]

$$N = \eta(\Theta, i^*) \left(\frac{F}{D} \right)^\chi e^{\frac{E_{i^*}}{(i^*+2)k_B T}}, \quad (2.9)$$

where $\eta = ((i^* + 2)\sigma_{i^*}\bar{\sigma}^{-(i^*+1)}\Theta)^{\frac{1}{i^*+2}}$ and Θ denotes the coverage. The exponent χ depends on the critical nucleus size i^* . In the case of isotropic diffusion the scaling exponent reads

$$\chi = \frac{i^*}{i^* + 2}. \quad (2.10)$$

The scaling relation (2.9) was confirmed experimentally by means of STM measurement, as e.g., in silver homo-epitaxial systems [18, 19]. In particular it could be used to determine the critical size i^* (by measuring N in dependence of F at fixed temperature T), and subsequently the activation energy of the adatom diffusion on the substrate surface (by measuring N in dependence of $1/T$ at fixed coverage Θ) [11, 20, 21]. Note that the applicability of the scaling prediction is restricted to low coverage $\Theta < 0.3$, and subsequently to both the intermediate nucleation regime (I) and the aggregation regime (A) (see Fig. 2.2). Following Amar and Family [22] the submonolayer growth can be classified into four typical time (coverage) regimes: (i) the low coverage regime (L), (ii) the intermediate coverage nucleation regime (I), (iii) aggregation regime (A), and (iv) the coalescence and percolation regime (C). Figure 2.2 shows that in the aggregation regime (A) the number density of stable islands remains approximately constant and afterward decreases strongly in the coalescence regime (C) due to coalescence of stable clusters.

Another quantity of particular importance characterizing the first stage in surface growth is the cluster size distribution (ISD). The ISD can be measured experimentally and contains important information concerning spatial dependencies. Based on both experimental and theoretical investigations [23, 24, 25], the ISD fulfills a scaling form

$$n_s = \frac{\Theta}{\bar{s}^2} f\left(\frac{s}{\bar{s}}\right) \quad (2.11)$$

in the pre-coalescence regime, and for large average island size $\bar{s} = \sum_{s>1} n_s/N \gg 1$. $f(x)$ denotes a scaling function for a given critical nucleus i^* and satisfies the normalization

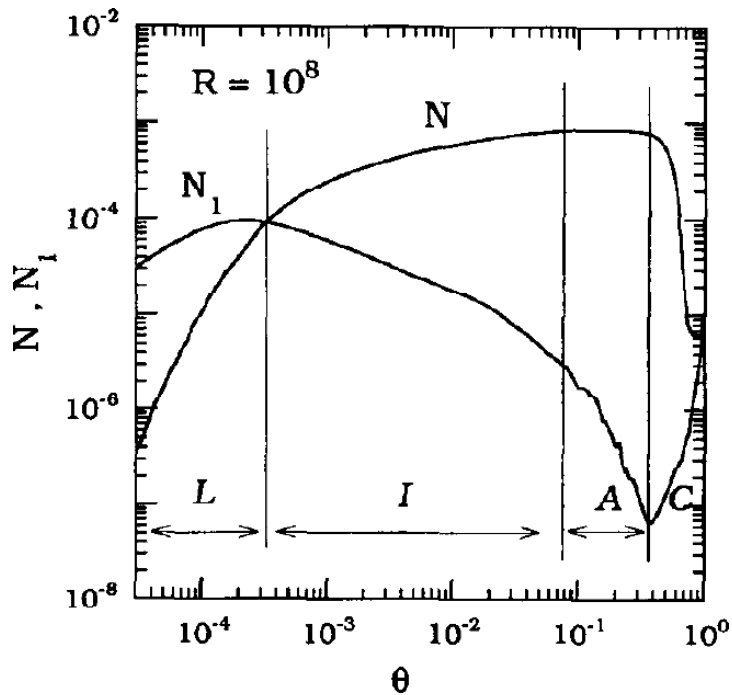


Figure 2.2: Typical behavior of the adatom density and the number density of island density (N) in submonolayer growth regime (taken from [22]). The indicated regimes are the low coverage nucleation regime (L), intermediate coverage nucleation regime (I), aggregation regime (A), and the coalescence and percolation regime (C).

condition

$$\int_0^{\infty} f(x)dx = \int_0^{\infty} xf(x)dx = 1 \quad (2.12)$$

where $x = s/\bar{s}$ is a dimensionless variable. Note the so far an exact analytical form for the scaling function $f(x)$ is not attainable. However, compared to experimental findings and extensive computer simulations, a reasonable empirical form

$$f(x) = C_{i^*} x^{i^*} \exp(-ia_{i^*} x^{1/a_{i^*}}) \quad (2.13)$$

was suggested by Amar and Family [12]. The parameters a_{i^*} and C_{i^*} can be obtained from the normalization conditions (2.12). Moreover, an explicit form of $f(x)$ can be calculated from the continuum version of underlying MFRE (equation 2.5) in the limit $\Gamma \rightarrow \infty$, (for review see [8], and references therein) if details of the capture numbers are assessable. It should be noted that the MFRE are not capable of producing the correct island scaling without the knowledge of the functional form of the capture numbers σ_s , whose size and Θ dependence is still an ongoing object of study [16, 26, 27].

In summary, despite the fact that the traditional mean-field treatment fails in predicting the correct form of the ISD, the MFRE are a valuable tool for the extraction of

microscopic quantities, like diffusion barriers and effective adatom binding energies, in combination with STM measurement of the number density of stable island N .

2.3 Ripening

Two-dimensional nanostructure rearrangements at a given temperature in the post-deposition regime are dominated by ripening processes. At nanoscale different ripening mechanisms are possible depending on the driving force. The post-deposition regime is characterized by microscopic balance between the “average-sized cluster” and the adatom density [28]. Thus clusters, which are either smaller or larger than the average cluster, are out of balance with the adatom density. More precisely, smaller clusters lose particles and larger cluster gain particles.

A well-known coarsening mechanism in the post-deposition regime is the Ostwald-ripening of droplets [29], where large droplets grow by the accumulation of diffusing particles from small evaporating droplets. As time proceed, the averaged droplet radius $R(t)$ grow, while their number decreases, but the volume fraction of the droplets remains constant. The analytical description of Ostwald-ripening, called as LSW theory, was developed by Landau and Slyozov [28, 30], and Wagner [31]. According to [32] there are two distinct regimes which are either governed by diffusion (diffusion limited (DL) mechanism [33]) or interface-transfer (aggregation limited (AL) mechanism [33]). That means if the diffusion is very fast, then the growth of grains is governed by the exchange of atoms at the perimeter of the cluster, i.e., the difference between adatom impact and dissociation. Otherwise the growth is dominated by diffusion and the difference of the adatom concentration at the cluster boundary and the average adatom density far away from clusters. In both cases the chemical potential is size dependent and still larger clusters grow at the expense of smaller ones.

Taking into account the mobility of islands and subsequently coalescence processes in the low coverage regime, in contrast to the Ostwald-ripening, a different coarsening mechanism takes places. This coarsening mechanism is called Smoluchowski-ripening [34] (cluster diffusion (CD) mechanism [35]). Here, mobility is assigned to clusters depending on their size. This assignment depends on the underlying dynamics that cause the macroscopic movement of clusters. There are three different regimes with different size dependencies. In the first case, cluster movement originates from peripheral diffusion (PD) [36], i.e., the cluster reorganizes through edge diffusion processes. In the second and third case the movement emanates from evaporation and recondensation of single adatoms, respectively [37]. The distinction relates to whether there is a larger energy barrier concerning the attachment of an adatom to a cluster edge or not. In the absence of such a larger barrier the cluster mobility is termed terrace diffusion (TD) [36] or correlated evaporation condensation. In the other case the evaporation and condensation are uncorrelated (EC) [36]. In table 2.1 all ripening mechanisms can be classified by their growth law (i.e. the scaling of the average cluster size as function of the observation time).

Coarsening (ripening) mechanisms		Scaling law
Ostwald	DL	$\langle s \rangle \sim t^{\frac{1}{3}}$
	AL	$\langle s \rangle \sim t^{\frac{1}{2}}$
Smoluchowski	PD	$\langle s \rangle \sim t^{\frac{1}{5}}$
	TD	$\langle s \rangle \sim t^{\frac{1}{4}}$
	EC	$\langle s \rangle \sim t^{\frac{1}{3}}$

Table 2.1: Growth law of the mean island size in dependence of time for the different coarsening mechanism. [28, 36].

In addition, there is another situation, which cannot be explained by means of Oswald-ripening. More precisely, the ripening mode of one-dimensional structures, where the dissociation rates are (nearly) independent of size [38] and thus the thermodynamic driving force (Gibbs-Thomson-effect) responsible for Ostwald-ripening is missing. The coarsening mechanism of one-dimensional structures is termed stochastic ripening (SR) [38, 39].

3 Growth of helicenes on calcite (104) surfaces

The search for systems that grow in one-dimensional structures is motivated by the advances made in molecular electronics and the foreseeable limit for further miniaturization of silicon technology. Two main structures, such as transistors and wires, are required to implement or create molecular electronics. While a molecule by molecule construction strategy is unfeasible [40], techniques involving self-assembly seem to be a promising approach for creating vast amounts of such structures. Currently there are numerous experiments which exhibit the growth of one-dimensional structures but they are conducted on metal or on semiconductor surfaces [1, 41, 42, 43, 44], and those are unsuitable candidates for molecular wires because of the conducting substrate.

In search of suitable material systems that utilize molecular self-assembly for creating one-dimensional molecular structures on insulating surfaces the group of A. Kühnle at the University of Mainz [7] found that a derivative of helicene exhibits wire-like structures on a calcite surface. This chapter begins with an explanation of helicene growth experiments on calcite (104) surfaces followed by a summary of main findings.

3.1 Experimental Setup

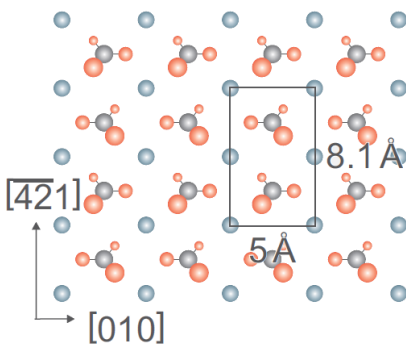


Figure 3.3: Schematic picture of the (104)-calcite cleavage plane taken from [7].

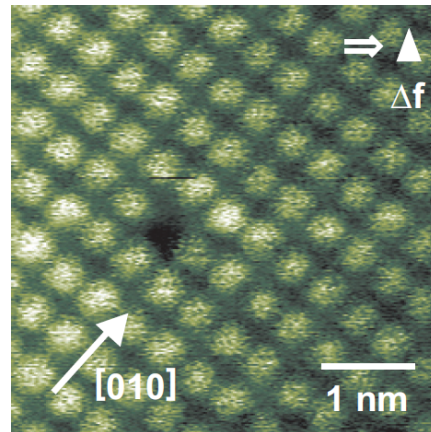


Figure 3.4: Atomic force microscopy image of the empty (104)-calcite plane taken from [7].

The self-assembled growth of organic molecules starts from an empty (104) cleavage plane of calcite (see figures 3.3 and 3.4). This plane has ditches along the [010] direction. After preparation (involving degassing, cleaving, and annealing [7]) the calcite surface has large, nearly defect-free terraces. In these experiments the used organic molecules are heptahelicene-2-carboxylic acids ([7]HCA). Details of the [7]HCA synthesis are given in [45]. [7]HCA molecules consist of seven phenyl rings with one of the ends functionalised with a carboxylic acid group. This leads to two enantiomers with different chirality,

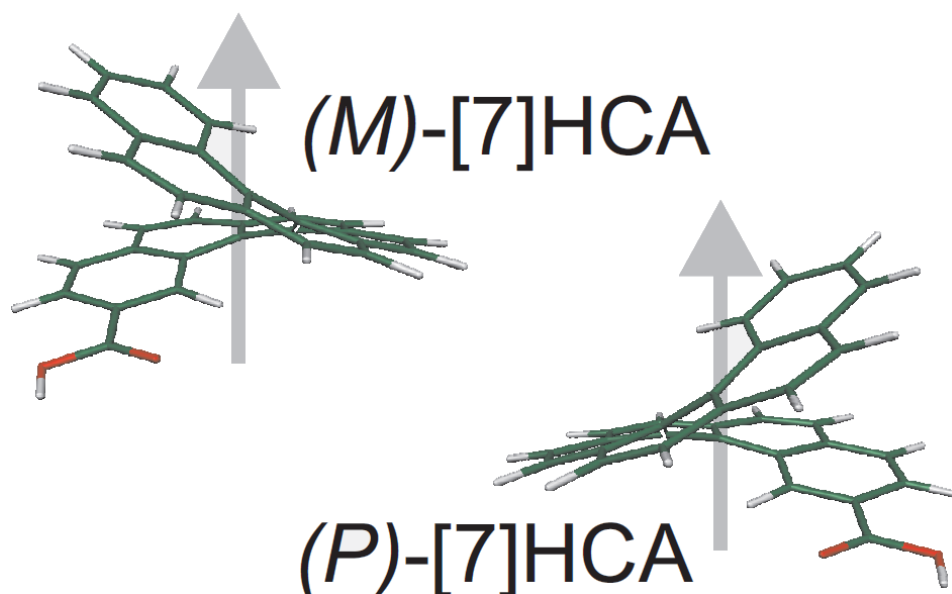


Figure 3.5: The helicene enantiomers in stick representation taken from [7]. The gray arrows indicate the helical axis.

depending on which end the functional group is attached. The structures are shown in figure 3.5. For short notation both structures are denoted as *helicene*. It is important to note that two different intermolecular interactions can be expected for this molecular structure. One could originate from the carboxylic acid group by the formation of hydrogen bonds and the other from interactions between the aromatic system of the seven phenyl-rings via π - π stacking. Due to the anisotropic molecular structure these bonds are highly directed.

It is known from previous studies of bare helicenes¹ on different surfaces [46, 47, 48] that the molecules may be attached in different modes to the underlying substrate. They could either lie flat on the surface, the helical axis is then parallel to the surface normal, or standing upright with the helical axis perpendicular to the surface normal. Between those extremes another attachment mode with an angle of 43° between surface normal and helical axis was observed for bare helicenes deposited on Ni(111)[7].

The deposition of [7]HCA molecules on calcite was carried out under UHV conditions at room temperature. After the deposition the surface was imaged by means of non-contact mode atomic force microscopy (NC-AFM) [7]. In figure 3.6 a surface image roughly six hours after the deposition is shown. As can be seen, the wire-like structures formed by the helicenes are on flat terraces and are of well-defined width. All of these self-assembled one-dimensional rows are directed along the [010] direction of the calcite surface. In addition, high resolution line scans on the helicene rows were performed to obtain information about their structure. In accordance with the interpretation of the

¹without additional functional groups.

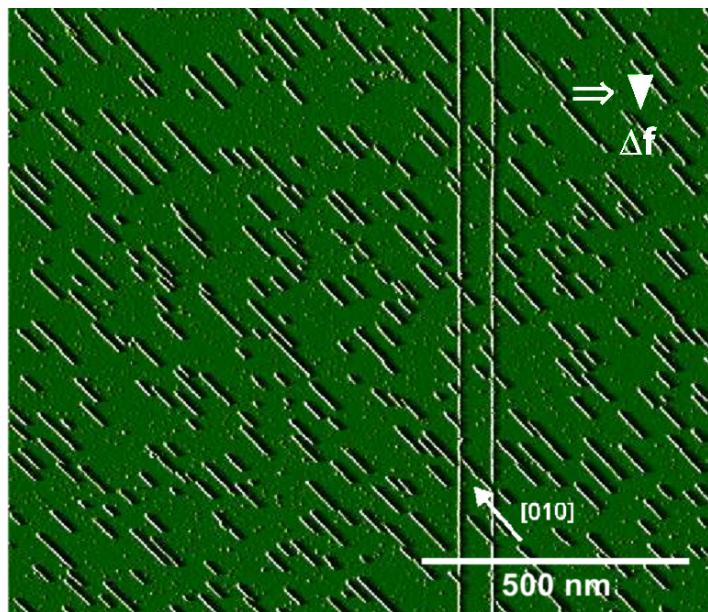


Figure 3.6: AFM image of the calcite surface six hours after helicene deposition. The coverage is around five percent. The arrow in the picture indicates the [010] direction, taken from [7].

AFM data, possible row formation structures with respect to the chirality of molecule pairs are evaluated by means of DFT calculations

3.2 Experimental findings

Based on AFM measurements the distribution of row lengths can be extracted and subsequently the mean length can be calculated in dependence of time². The AFM images taken shortly after the deposition show two distinct row species, broader and narrower ones.

In figure 3.7, taken one hour after the deposition, some of the thin rows are indicated. The broader rows are approximately twice the width of the thin ones, indicating that the thin rows consist of single molecules and the broader of dimerized species, and that single molecular rows are less stable than the dimerized ones, because of their absence at later times³. This is furthermore supported by DFT calculations, which yield a very small binding energy for single molecular rows (0.09 eV) compared to the molecular row-pairs (≈ 0.3 eV) [7]. For the pairs two different realizations are possible: they are either arranged heterochiral, which means the pairs consist of molecules with different chirality, or homochiral, where both molecules have the same chirality. The computed energy values for these conformations differ only slightly [7]. Besides values for bind-

²The (unpublished) data in Fig. 3.8 and 3.9 are provided by P. Rahe (University of Mainz).

³The broader species were already shown in figure 3.6 six hours after deposition.

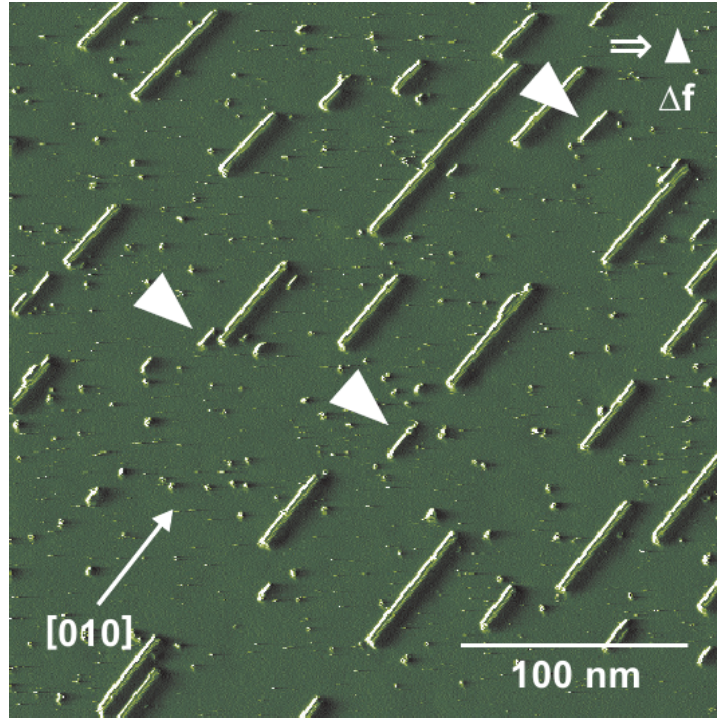


Figure 3.7: High resolution image of the calcite surface one hour after helicene deposition taken from [7]. Thin rows are indicated by arrows.

ing energies, the distance between two dimer unit cells can also be obtained from DFT calculations, which were performed in vacuum without considering the influence of the substrate [7]. These calculations yield a distance of 7.3 \AA for helicene molecular pairs.

The height of the rows was measured and is approximately 7 \AA with respect to the surface [7]. Taking into account that the molecules are roughly 11 \AA in height (see figure 3.5) this indicates a tilting angle of the helical axis with respect to the surface normal. Compared to the distance of repetition units along the helicene rows, which was determined to be 10 \AA [7], and the assumption of a tilting angle of around 45° , as found in the studies on Ni (111) [7], the distance between the molecular pair repetition units evaluates to around 7 \AA and the height to around 8 \AA . This reproduces the equilibrium distance for isolated molecular pairs of helicene quite well and also coincides with the measured height [7].

In figure 3.8 measured length distributions at a coverage of 6 % are shown. There is a distinct peak at intermediate length and the distributions become slightly broader during time. The peak of the histograms is slightly shifted to larger lengths. As can be seen from figure 3.8, the measured mean length $\bar{L}(t)$ reveals three distinct regimes: (I) a *deposition regime* for times t smaller 600 s, (II) a *strong ripening regime* in the range $600 \leq t \leq 5000$ s, (III) a *saturation regime* at long times.

In regime (I) the helicenes are deposited on the substrate and form quasi one-dimensional (wire-like) structures. For the shown images, helicenes were deposited for ten minutes at a deposition rate of $10^{-4} \frac{\text{ML}}{\text{s}}$ [7]. Note that during this regime no AFM measurements are possible. After finishing the deposition a rather strong coarsening of the wire-like helicene structures can be observed, i.e., $\bar{L}(t)$ increases linearly in time. About 80 minutes after the deposition a crossover from regime (II) to regime (III) takes place. In Regime(III) the mean length of wire-like helicenes remains nearly constant, i.e. it saturates.

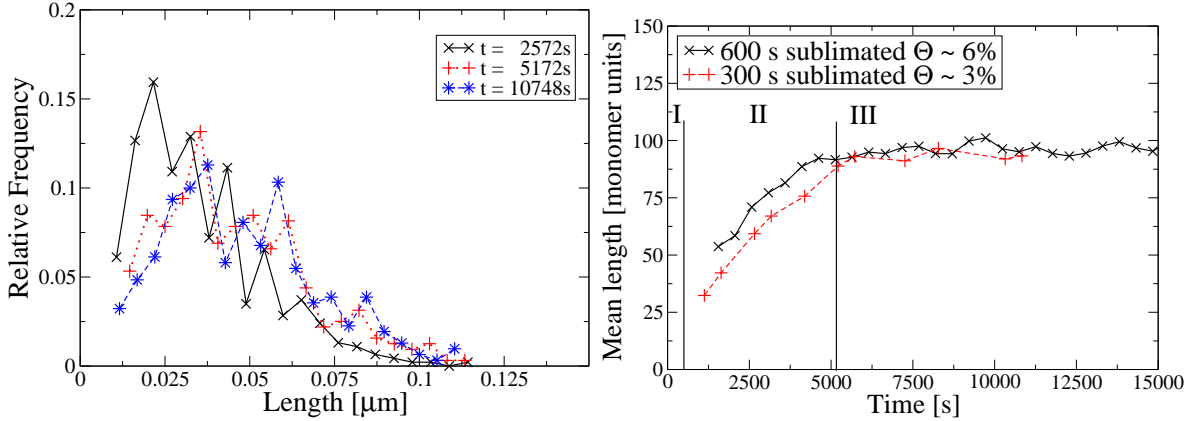


Figure 3.8: Measured length histograms at a coverage of roughly 6 %.

Figure 3.9: Mean length measurement of the helicene structures. The indicated regimes are: (I) deposition regime, (II) strong ripening regime, and (III) saturation regime.

The observation of the structures indicates anisotropic interactions and only molecules inside of the pairs are affected by the hydrogen bonding. Otherwise compact or at least broader islands would grow if an attachment perpendicular to the row growth was worthwhile. The indicated thinner rows in figure 3.7 suggest that the creation of dimerized species does not happen instantaneously when two monomer particles meet on the surface. Furthermore follows that within a helicene row the helical axis points in the [010] direction, therefore molecules will feel only strong attractive forces of the π -system if they are at one of the row's ends. Because of the anisotropy of the (104) cleavage plane of calcite, the diffusion is assumed to be anisotropic as well. The group of A. Kühnle also gives an estimate for the diffusion energy barrier. They observed single molecules after deposition on the substrate at 110 K; at that temperature no diffusion occurs and the molecules stick on the initial deposition site. Therefore a range for E_D from 0.4 eV to 1.0 eV was estimated [7].

In summary, from the experimental observations, we can deduce the following properties of the helicene structure formation on calcite (104):

- stable rows consist of dimers

- monomer encounters do not necessarily lead to the creation of dimers
- the molecules in the rows have a tilting angle
- the helical axis points along the [010] direction
- the diffusion is anisotropic
- anisotropy of the adatom-adatom interactions
- two ripening regimes, denoted by (II) and (III) respectively, with different slopes of $\overline{L}(t)$ as function of time t in the post-deposition.

The observed ripening behavior of the mean length $\overline{L}(t)$ gives rise to the questions: *(i)* what is the crucial process responsible for the ripening (coarsening) behavior of wire-like helicene structures on a two-dimensional insulating substrate in regime (II), *(ii)* what leads to its end, to saturation. Due to the fact that two different row species are observed experimentally, it seems, in this context, an important issue to clarify the interplay between monomer and dimer species and subsequently their influence on the grow and coarsening kinetics in the post-deposition regime.

4 Growth modeling

In order to understand the underlying growth and ripening mechanisms of the experimental findings in the post-deposition regime in Sec. 3.1, several models were designed. The complexity of these models was increased when there was no possibility to match the experimental data with any set of reasonable parameters. The idea was to start with a minimal model able to form one-dimensional (wire-like) structures, so that the extension of the model when adding new processes through new interactions could be justified. So if a newly introduced process is able to form a model that fits with the experiment, it should be the one with the least additional processes and therefore only contain crucial additional assumptions.

4.1 Basis model

In general the models belong to the family of lattice-gas simulations [49, 50], hence the underlying grid is discrete in space. Every site can be occupied by only one particle, which later on will be identified as monomer or dimer, respectively. The simulation starts with an empty terrace, on which particles are deposited randomly on the free surface with flux F . Funneling [51, 52] is not taken into account, which is valid for low coverages Θ , where direct impingement is negligible. Therefore deposited particles perform free diffusion [53, 54] with rate D_0 and the corresponding energy barrier E_D until they aggregate on an island or nucleate with another particle. As already mentioned in Sec. 2.1, the diffusion rate reads

$$D_0 = a^2 \nu e^{-\frac{E_D}{k_B T}}. \quad (4.1)$$

In what follows, we set the hopping distance $a = 1$. The interactions between particles are modeled with the bond-counting method [55, p. 298]. Hence the different configurations before and after a jump, in particular the difference of direct neighbors, have to be considered. Thus, the diffusion (more precisely jump) rate reads

$$D_{M/D}^\alpha = \nu e^{-\frac{E_D^\alpha}{k_B T}} e^{-\frac{1}{2}(n_i - n_f)E_B^{M/D}} \equiv D_{0M/0D}^\alpha e^{-\frac{1}{2} \frac{\Delta E^{M/D}}{k_B T}} \quad (4.2)$$

where $\Delta E^{M/D} = (n_i - n_f)E_B^{M/D}$ is the energy difference between the initial and the final state, n_i and n_f are the numbers of neighboring particles, which are connected by the binding energy $E_B^{M/D}$, in the initial and final state, respectively. $D_{0M/0D}^\alpha$ is the diffusion rate for free particles (monomers and dimers, see equation 4.1) for the respective direction $\alpha = 1, 2$ ⁴. Hence, the diffusion anisotropy is determined by ratio between the energy barriers E_D^1 and E_D^2 . Additionally the anisotropy of the interactions are also included, because direct neighbors of only one direction are considered. This direction, which is associated with the binding energy $E_B^{M/D}$, coincides with the row growth. The

⁴The upper index α denotes the jump direction, i.e., $\alpha = 1$ for jumps in the direction of the row growth and $\alpha = 2$ for jumps in the direction perpendicular to the row growth.

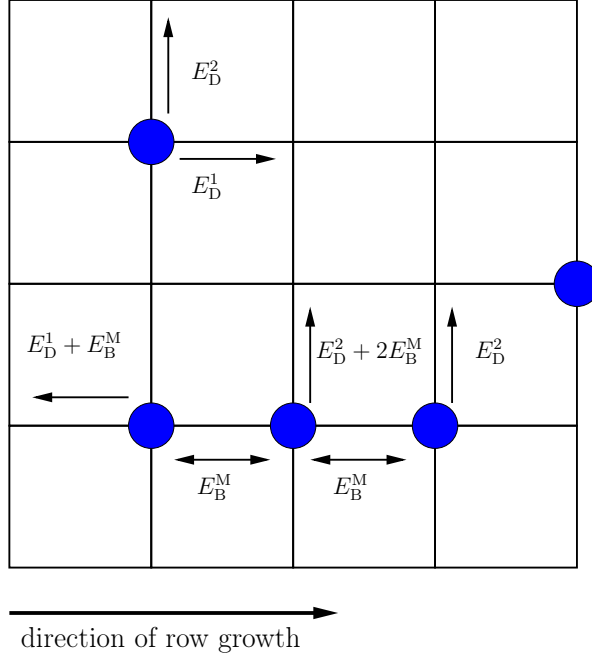


Figure 4.1: Processes involved in the basis model (Model I 4.4).

main jump processes, which are specified by their energy barriers, are depicted in figure 4.1. As explained in section 7.1 such processes are collected in classes and are updated around affected sites in every time step. In the upper left corner of figure 4.1 a free diffusing particle is shown with the energy barriers E_D^1 for diffusion in and E_D^2 for diffusion perpendicular to the row growth direction, thus $\Delta E^M = 0$. Below a group of three connected monomers is shown with their associated binding energies and diffusion barriers drawn right next to them. The particle on the left dissociates from the row in the direction of row growth and loses one next neighbor, hence the whole energy barrier for this process is $E_D^1 + E_B^M$. The particle in the middle is bound twice and escapes the row perpendicular to the row growth, hence the overall barrier is two times the monomer binding energy E_B^M and the diffusion energy barrier E_D^2 . The particle to the right also escapes perpendicular to the row growth, but has no net loss of next neighbors in the direction of row growth, thus the rate for this jump process is determined solely by the associated diffusion barrier E_D^2 .

4.2 Edge diffusion (ED)

Questions related to the ripening process of wire-like helicene structures on a two-dimensional substrate in the post-deposition regime might be closely related to an edge-diffusion process. Because each wire can, independently of their length, only gain or lose two helicenes at their ends. The capture of helicenes perpendicular to the grow direction of the rows in dependence on the wire-length, accompanied with an edge diffusion process along the wires, enables a coarsening (ripening) of wire like structures on

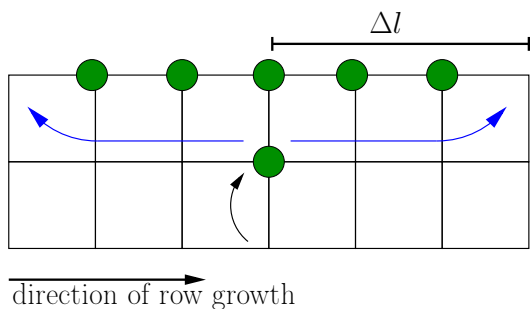


Figure 4.2: Edge diffusion after a jump perpendicular to the row growth direction.

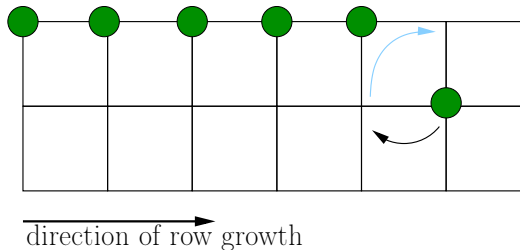


Figure 4.3: Edge diffusion after a jump in the row growth direction.

a two-dimensional substrate.

There are several possible simplifications for this process, which will be discussed thoroughly. One has to consider the type of the particle, which is involved in edge diffusion, as well as the row type, on which this process takes place. The possibilities in question are monomer particles (M) partaking in edge diffusion on either monomer or dimer rows and dimer particles (D) partaking in edge diffusion on also either monomer or dimer rows. The case of dimers conducting edge diffusion on monomer rows is very unlikely, because of the smaller diffusion rates of dimers and thus is, in general, less important and therefore neglected. Nonetheless edge-diffusion of dimers on dimer rows will be considered in case of mobile dimers. Note that there is also another criterion, which distinguishes edge diffusion processes. A helicene molecule that jumps perpendicular to the growth direction can hit a site, which is adjacent to an existing row as shown in figure 4.2. This case will be treated individually, because several variations for the implementation are possible. In contrast to this, for the case of edge diffusion after a jump in the row growth direction, it is only important if the combination of the edge diffusing particle and the row is allowed for this process. So if edge diffusion is included as a process the implementation for the latter case will be the same. A possible configuration for this process is shown in figure 4.3. For this process it is important to note that edge diffusion takes place only if there are neighbors of the right type, adjacent to a site that would have been occupied if there was no edge diffusion permitted. As a consequence the moving particle in figure 4.3 does an actual jump to the position indicated by the black arrow. It is then checked whether the rules defined for edge diffusion apply, and if so the particle is moved to the site indicated by the blue (light gray) arrow. The last move, the edge diffusion, happens instantaneously, so for this kind of move no time is used and therefore its rate is infinitely large. This treatment has the advantage that no extra energy parameter is used but at the same time this treatment violates the detailed balance.

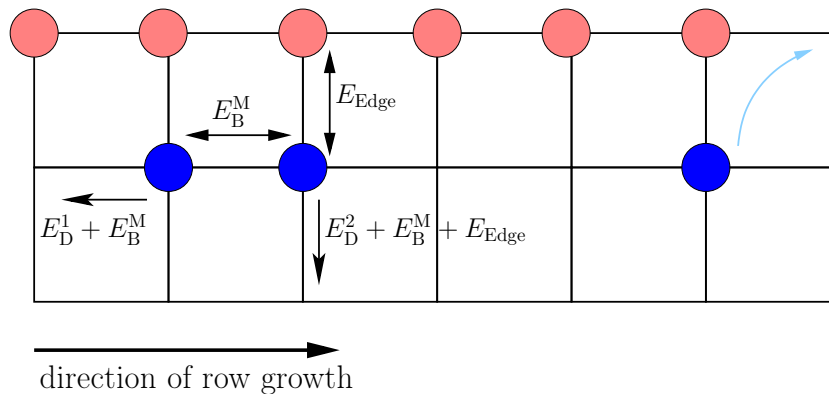


Figure 4.4: Processes involved for the implementation of slightly aided edge diffusion. Blue monomers, red dimers.

4.2.1 Standard edge diffusion mechanism

A common possibility for the implementation of edge diffusion is a mechanism that works through coupling the edge diffusing particle with its corresponding row or edge. Now a particle that hits a row after a jump perpendicular to the row growth direction, is affected by an attractive potential, so that the rate for jumps away from the row are decreased and the particle then diffuses along this row until it finds an end, completing the edge diffusion, or hops away. Consequently the detailed balance within this variant is nearly unperturbed. But there are some open questions like the treatment of two particles that meet at the same row or the energy barrier for diffusion along a row. In the framework of this thesis the diffusivity for such particles is not enhanced and the interaction is handled the same way as between particles that meet afar from such a row. Furthermore dimer edge diffusion was neglected entirely and also the edge diffusion from a monomer on a monomer row was not considered. Therefore only the processes shown in figure 4.4 were added to the elementary processes explained in the previous Sec. 4.1. Monomer particles are bound with E_{Edge} to dimer rows and diffuse with the energy barrier E_{D}^1 as previously. If they jump in the vicinity of another monomer they are bound with the monomer binding energy E_{B}^{M} , and the effective barrier is increased by the binding energy as shown in figure 4.4. Jump rates away from the row involve possible binding energies E_{B}^{M} from neighbors and the diffusion barrier E_{D}^2 , which is additionally increased by the energy E_{Edge} . Another important implementation feature has to be pointed out, if the end point of a row is occupied by a monomer and another monomer reaches that end via edge diffusion, a dimer is created right after the jump around the corner. Thus the dimer creation barrier E_{Barrier} (see Sec. 4.3) has no effect in this case.

4.2.2 Instantaneous edge diffusion

As briefly mentioned above the edge diffusion which can occur after a jump along the row growth direction is always handled in a instantaneous fashion. In the implementation described in this section the edge diffusion after jumps in the other direction will

be treated in the same way. That means when a particle hits a row after a jump perpendicular to the row growth, it is instantaneously moved to one of the end points. If there is such a row, the ends of it are detected and then the particle is moved to the shortest end. For the models without dimer structures the row-ends are empty sites. For the models involving dimers, however, the ending points are defined as the sites which are occupied by a particle different from the initially hit one. Now one has to choose whether sites already occupied with a single helicine can be the target of another one. For this work this is only allowed if the row that was hit consists of dimers and the edge diffusing particle is consequently a monomer. The dimer creation after edge diffusion is not affected by the dimer creation barrier E_{Barrier} (see Sec. 4.3).

To sum up, the possible realizations for edge diffusion are:

1. A monomer on a monomer row
2. A monomer on a dimer row
3. A dimer on a dimer row

This approximation is rather crude especially for cases when a large row is hit which causes a big distortion to the system in terms of the equilibrium dynamics. Because the bigger the leap between the point of the initial contact with the row and the destination point is the more time would be needed in a real system to overcome this distance. It is also likely that a particle jumps away from the row before it reaches an end in the case of large distances.

4.2.3 Edge diffusion limited by maximum distance

For this implementation the same ideas as pointed out in the previous section 4.2.2 apply. The difference is that now the edge diffusion is conducted only if the distance between the initial contact point and one of the end-points are within a given limit. This limit is derived from the mean square displacement after a particle hits a row. The mean time a particle remains at this edge (row) is

$$\tau = \frac{1}{D_{\text{OM/OD}}^2 e^{-\frac{E_{\text{B}}}{k_{\text{B}}T}}} \quad (4.3)$$

with the energy E_{B} , which binds the particle to the row and is different from the in-row binding energy $E_{\text{B}}^{\text{M|D}}$, and $D_{\text{OM/OD}}^2$ the free diffusion rate perpendicular to the row growth. Per definition the mean square displacement in one dimension for a given time τ is

$$\langle x^2 \rangle = 2\tilde{D}_{\text{OM/OD}}^1 \tau \quad (4.4)$$

with $\tilde{D}_{\text{OM/OD}}^1$ as diffusion rate for edge diffusing particles. Because both new parameters, E_{B} and $\tilde{D}_{\text{OM/OD}}^1$, are unknown and would increase the parameter space in an unnecessary

manner for obtaining a simple estimate, the jump rates for free diffusion are used instead. Thus

$$\Delta l_{\max} = \sqrt{\langle x^2 \rangle} \approx \sqrt{2 \frac{D_{0M/0D}^1}{D_{0M/0D}^2}} \quad (4.5)$$

is used as the upper limit for the leap that edge diffusion can overcome as depicted in figure 4.2. The jump rates for free diffusion $D_{0M/0D}^1$ (in-row growth direction) and $D_{0M/0D}^2$ (perpendicular to the row growth) are defined in equation 4.2. If the dimers are mobile the same limit applies because the ratio between the diffusion rates is same as for the monomers (cf. section 4.3).

For edge diffusion that occurs after a jump in the row growth direction the distance that has to be overcome is always one. Another consequence of this definition is that in the case of isotropic diffusion Δl_{\max} tends to one as well⁵. Therefore this implementation limits effectively the perturbation that would be caused by unreasonable big leaps. Nonetheless detailed balance is not absolutely ensured as it would be in the absence of edge diffusion. However as will be shown later, edge diffusion is crucial for the dynamics of the experimental system and the realization of edge diffusion in this manner proves to be a fairly good approximation. Like in the variant of the previous section 4.2.2 one can distinguish between different allowed particle interactions and the same cases as before are applied.

4.3 Dimerization

In order to include the experimental observation of dimer structures [7] a respective implementation was developed. The main ideas behind the simulation remain the same as in the previous case but now dimer structures are introduced. This is accomplished through double occupation of lattice sites. There are several parameters necessary to characterize interactions concerning dimer structures. Firstly dimers are expected to have a different energy barrier for diffusion, those are denoted with E_D^3 for jumps in the row growth direction and E_D^4 for jumps perpendicular to the row growth. Second, there is a binding energy E_{Dimer} relevant to the dimer structures, which is important for the creation and dissociation of dimers, as shown in figure 4.5 in the middle right part and the lower left corner. The parameter E_{Barrier} does influence only the creation of dimers (indicated by (**) in figure 4.5) and is used merely to adjust the rate of dimer creation. Hence a high value slows down the creation of dimers considerably. Without this parameter nearly every encounter of two monomers would result in a dimer, which is not observed in the experiments [7]. Now, $k_{\text{Dimer}} = D_{0M}^\alpha \exp(-E_{\text{Dimer}}/k_B T)$ ⁶ defines the rate with which free dimers dissociate. Here, E_{Dimer} is an additional energy barrier, which has to be overcome when a dimer dissociates (indicated by (*) in figure 4.5). At the same time it influences the creation of dimers because it occurs together with E_{Barrier}

⁵More exactly this limit will be $\sqrt{2}$, because of the discrete grid this is rounded to 1.

⁶with $\alpha = 1,2$ for the both jump directions as before.

so the dimer creation rate is governed by the difference $E_{\text{Barrier}} - E_{\text{Dimer}}$. There is one further parameter associated with the dimer structures, the binding energy between two dimers next to each other in the direction of row growth E_B^D . In the framework of this thesis it is assumed that this value is related to the binding energy between monomers via $E_B^D = 2E_B^M$. As depicted in figure 4.5 at the lowest line it is possible for monomers and dimers to interact with each other. The binding energy in such a case is the monomer binding energy E_B^M . As a consequence a dimer bound to other dimers can dissociate by overcoming an energy barrier of $E_{\text{Dimer}} + E_D^\alpha + E_B^M$, therefore losing only the monomer binding energy and the internal dimer binding energy. It should also be noted that for dissociation the monomer diffusion barrier is used⁷. This originates from the notion that microscopically two neighbored dimers are like four monomers bound to the respective neighbor at the next site and the monomer at the same site with E_{Dimer} , so each of these monomers can jump away overcoming only the respective monomer binding energy at the corresponding site.

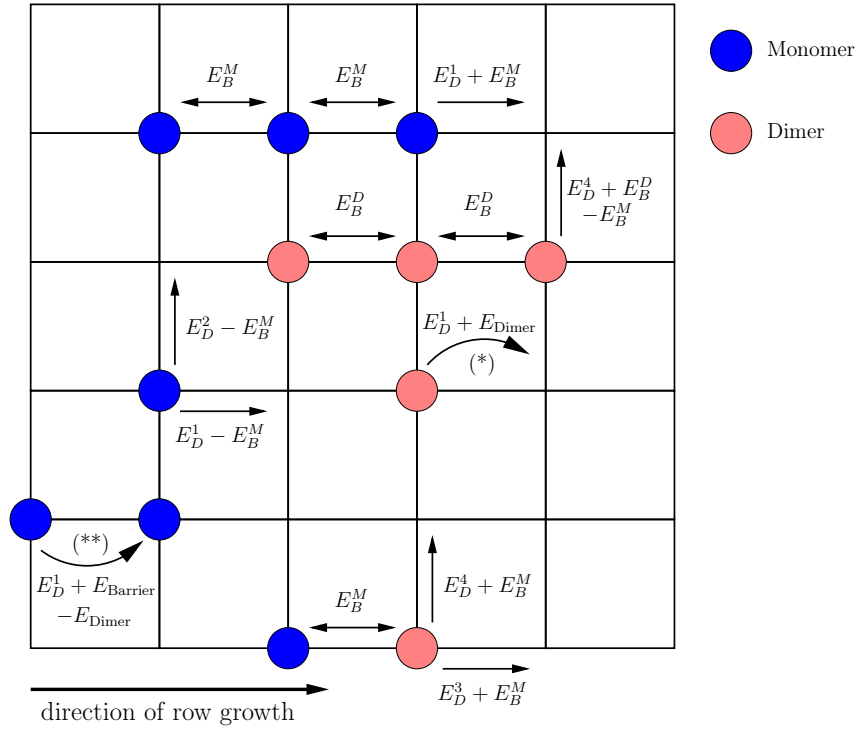


Figure 4.5: Main processes of the simulation model with dimer structures.

The diffusion barriers for the dimers are not chosen independently but rather calculated from the free monomer diffusion rate. The ratio of the diffusion along the growth direction to the direction perpendicular is the same for monomers and dimers: $\frac{D_{0M}^1}{D_{0M}^2} = \frac{D_{0D}^1}{D_{0D}^2}$. This decision is arbitrary but decreases the number of independent parameters and the

⁷ E_D^α with $\alpha = 1, 2$.

surface anisotropy affects the dimer diffusion in the same way as it affects the monomer diffusion. In order to provide a model with the least possible complexity the dimer diffusion can be rendered unimportant if the factor DR is set to very large values. Edge diffusion may be added to this implementation. Based on the microscopic processes, introduced in section 4.1-4.3, the following models emerge concerning different levels of a description.

4.4 Model I: Monomers (M)

This model includes only the processes listed in section 4.1. Hence edge diffusion and dimer particles are not considered.

4.5 Model II: Monomers and instantaneous edge diffusion (MIE)

This model adds the instantaneous edge diffusion mechanism to the model I as explained in section 4.2.2. Everything else remains unchanged.

4.6 Model III: Monomers and edge diffusion limited by maximum distance (MLE)

For this model the distance, which an edge diffusing particle can overcome, was limited according to the rules explained in section 4.2.3. So the edge diffusion mechanism limited by a maximum distance was added to model I.

4.7 Model IV: Including dimer structures (D)

As the name implies particles in the simulation are allowed to form dimers as explained in section 4.3. In this first model that incorporates dimer structures any edge diffusion is omitted.

4.8 Model V: Dimers and conventional edge diffusion (DCE)

Similar to the strategy used by the models without dimers various edge diffusion realizations were implemented additionally. This model expands model IV with conventional edge diffusion as explained in section 4.2.1.

4.9 Model VI: Dimers and instantaneous edge diffusion (DIE)

This implementation expands Model IV with additional instantaneous edge diffusion as explained in section 4.2.2.

4.10 Model VII: Dimers and edge diffusion limited by maximum distance (DLE)

In order to limit the possible distortion caused by the instantaneous edge diffusion algorithm the maximal distance a particle, either monomer or dimer, can overcome was limited according to the rules introduced in section 4.2.3.

4.11 Model parameters

To evaluate these models, kinetic Monte Carlo (KMC) simulations are performed. Table 4.1 summarizes the parameters used in the KMC simulations and additionally shows the ranges or values for these parameters, respectively. The ranges for the parameters are derived from the estimates given by Rahe et al. [7]. From these energy values the

Symbol	range	description
M	2048	length of simulation area
T	300K	temperature
ν	$10^{10} \frac{1}{s}$	attempt frequency
E_D^1	0.3...0.5eV	energy barrier for diffusion in growth direction
E_D^2	0.3...0.5eV	energy barrier for diffusion perpendicular to growth direction
E_D^3	0.3...0.5eV	energy barrier for dimer diffusion in growth direction
E_D^4	0.4...0.6eV	energy barrier for dimer diffusion perpendicular to growth direction
E_B^M	0.1...0.3eV	binding energy for monomers along growth direction
E_B^D	0.2...0.6eV	binding energy for dimers along growth direction
E_{Barrier}	0.6...2.0eV	energy barrier for forming dimers
E_{Dimer}	0.4...0.6eV	binding energy of dimer
DR	1...1000	ratio of monomer diffusion rate to dimer diffusion rate
F	$10^{-4} \frac{ML}{s}$	deposition rate

Table 4.1: Summary of parameters used in kinetic Monte Carlo simulations.

diffusion rates or in general every rate for possible processes are derived. The attempt frequency ν was chosen according to the results found in [56] where a value of around $10^{10} \frac{1}{s}$ was measured for a larger organic molecule. A change in this value results in an energy-shift of the diffusion energy-barriers. So instead of changing the attempt frequency an appropriate change could have been made on the diffusion barriers. But in order to get values around 0.4 eV for the diffusion barrier the attempt frequency was adjusted accordingly and the chosen value of $\nu = 10^{10} \frac{1}{s}$ fulfills this purpose.

It should also be noted that the diffusion barriers for dimers are not used explicitly during the simulation but are useful for the process characterization and are defined by the monomer diffusion rates and the factor DR because in the framework of this thesis it is assumed that the diffusion rate for dimers differ only by a factor of DR for both surface directions. So if those energy barriers for dimers were included explicitly they

both would only be shifted by the same energy value compared to the monomer activation barriers. This decision was made to reduce the number of independent parameters.

Also important is the parameter E_{Barrier} because there is no direct counterpart in the experiment. This parameter is used to adjust the rate of dimer creation and originates from the notion that the dimer bond, the hydrogen bond, is directional and therefore two meeting monomers need to rotate in the correct position in order to form the bond. So an encounter of two monomers need not necessarily lead to dimerisation. In the simulation however two meeting monomers would instantly form a dimer if they do not have to overcome an additional barrier. Unfortunately there is no information about the rate of dimer creation available nor is known if there are any free diffusing dimers, i.e. if this rate has to be considered at all. The measurements reveal only that at later times there are only a few remaining chains of monomers and the other chains all consist of dimers [7]. Yet alone the presence of monomer rows indicates that encounters of monomers do not instantly create dimers and therefore the introduction of an adjustable *dimer creation rate* is justified.

5 Results of growth simulations

In this chapter the results obtained from the KMC-simulations will be presented. The simulation area used in this work contains 2048×2048 lattice sites, i.e., $M = 2048$. The results are arranged in subchapters, one for each model introduced in section 4 and a final section that compares the models to each other. In each subsection snapshots from the simulation will be discussed, showing a 150×150 snippet of the simulation area. Furthermore the mean length depending on the simulation time as well as the island size distributions (ISD) are presented. For the models considering dimers the progression of the ratio of dimer particles on the whole coverage will be shown additionally. In contrast to the lattice periodicity in the [010]-direction with a unit-cell distance of 5 \AA a value of 10 \AA is used, according to the experimentally measured repetition length of the helicene rows [7]. Thus 10 \AA is the length a particle occupies in the simulation ('monomer unit'). The small green bar indicates the scale of the snapshots for the important [010] direction and is always 5 nm (5 monomer units) in length. The snapshots are chosen for two different times, which belong either to the experimentally observed regime with strong ripening (4000 s) or to the saturation regime (10000 s). The models without dimer structures are shown for two different binding energies E_B^M at the earlier time instead.

Furthermore the best approximation of the experimental data for each model will be presented in the following sections. This means the ripening behavior of the mean length of the grown structures will be investigated and compared to the experimental findings as presented in article [7]. The group of A. Kühnle offered their measured mean length data as well as the measured size distributions from which the mean length was calculated. For the comparisons the data set with roughly six percent coverage ($\Theta = 6\%$) were used.

5.1 Model I

In figure 5.1 and 5.2 snapshots of the simulation considering only monomer type particles with no edge diffusion are shown for two different binding energies at 4000 seconds simulation time, which corresponds to one hour after the deposition. On the left side the binding energy E_B^M was set to 0.18 eV , the value assumed for the interaction between two monomers next to each other, and on the right side the binding energy E_B^M was set to 0.36 eV , thus representing the interaction between the dimerised species. In both cases one-dimensional growth is achieved. The case with the larger binding energy yields longer islands due to the greater stability.

In figure 5.3 the mean length progression of this model is shown along with the experimental data and some interesting cases. It is clearly recognizable that the agreement between the simulation and the experiment is rather poor. The mean length as found in the simulation grows rapidly during the deposition and stays nearly constant or increases very slowly afterward. The two curves with the lower in-row binding energy (set (a) and (b) in Fig. 5.3) seem to show a very weak regime of "stronger ripening" right after the

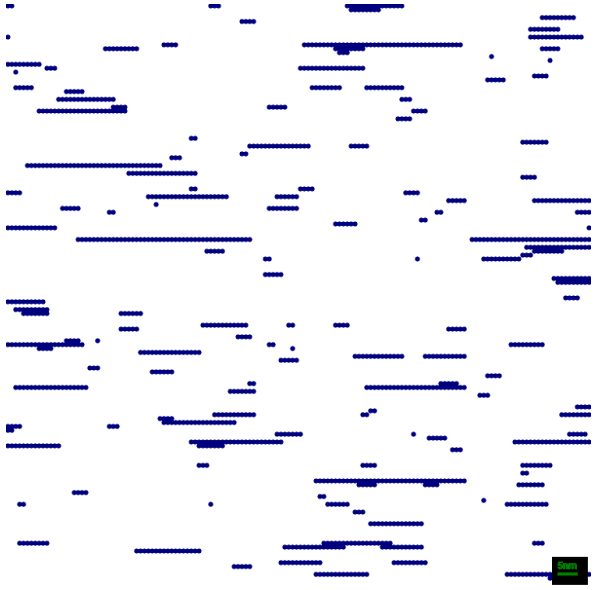


Figure 5.1: Simulation snapshot without dimer structures and without any edge diffusion at 4000 s. The in-row binding energy E_B^M was set to the 0.18 eV.

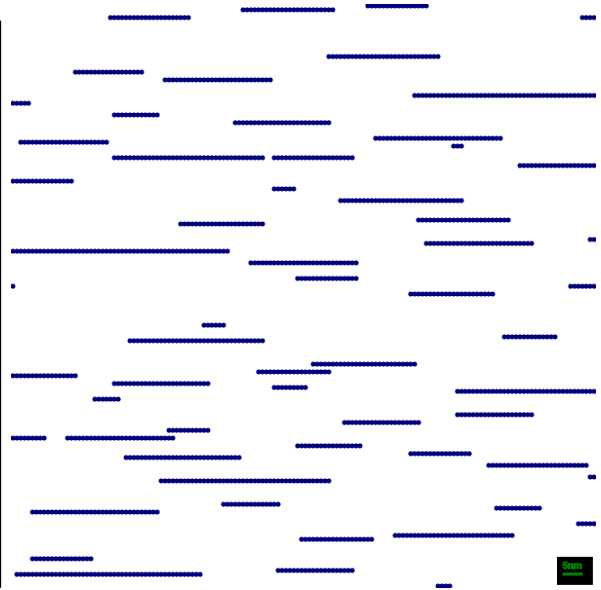


Figure 5.2: Simulation snapshot without dimer structures and without any edge diffusion at 4000 s. The in-row binding energy E_B^M was set to the 0.36 eV.

deposition, however their shape is not as distinct as in the experimental results. This is the main discrepancy between this model and the experimental data. Mean lengths well above and below the experimentally observed could be produced. This way only the regime of saturation could be reproduced. Simulations with *model I* typically yielded mean-length progressions with this distinct kink right after the deposition. Despite the rather poor accordance with the experiment, the behavior of the mean length indicates stochastic ripening [57]. But the ripening regime of this model is far too narrow.

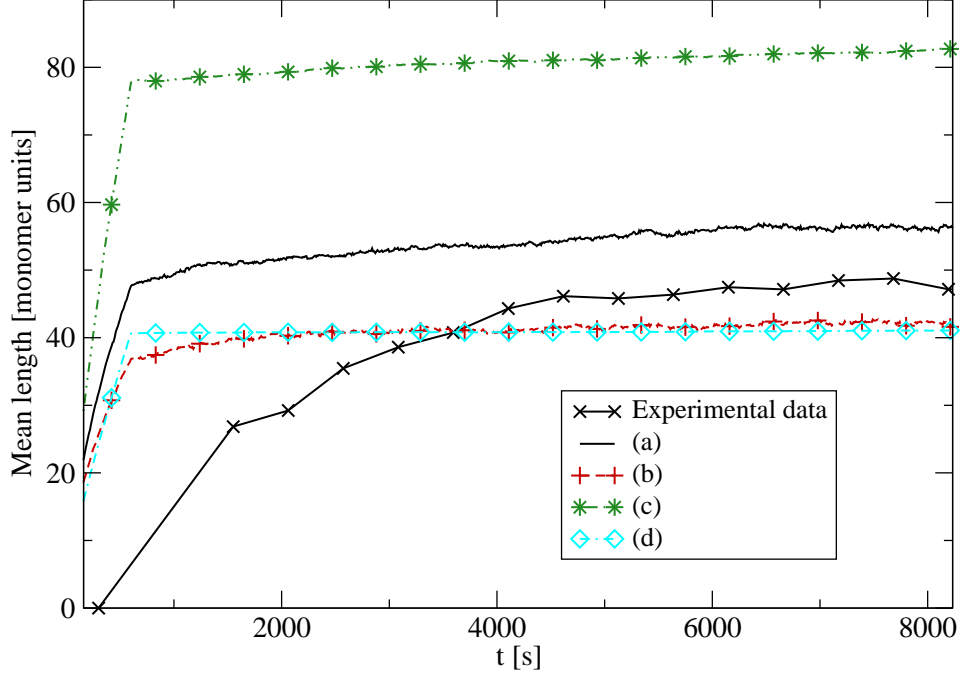


Figure 5.3: Comparison of the mean length from the model without considering dimer particles and edge diffusion with the experimental data. The black solid line represents the simulation data, which agrees well within the model restraints. The parameters for the best match (a) are: $E_D^1 = 0.34$ $E_D^2 = 0.42$, $E_B^M = 0.28$. For (b) the binding energy is lower (0.26 eV), for (c) higher (0.37 eV) and set (d) combines diffusion barriers which are higher ($E_D^1 = 0.40$ and $E_D^2 = 0.46$) with a larger binding energy ($E_B^M = 0.40$).

5.2 Model II

In figures 5.4 and 5.5 results of the simulation with additional instantaneous edge diffusion are shown one hour after the deposition. This time the simulation with the lower binding energy yields larger islands. Thus the growth is enhanced by the edge-diffusion mechanism and the lesser stability of the rows in the left picture increases the effect. The islands partially exceed the area of the extracted simulation snippet. Hence *model II* tends to produce extremely large rows if the binding energy within the rows is low. Already at this point the reliability of this edge diffusion implementation is questionable, because with the increasing length the distance a particle can travel through edge diffusion also becomes very large. Thus the deviation to *real* systems increases and the results may become unphysical. In addition to that the large lengths of those islands could lead to unwanted finite size effects. To counter that effect the simulation areas for this model were increased.

In figure 5.6 distinct results for the mean length of this model are presented. An obvious difference to the model without any edge diffusion (section 5.1) is that exceedingly large mean lengths can occur. Despite that, set (b) and (c) share a common property with the



Figure 5.4: Simulation snapshot without dimer structures and with instantaneous edge diffusion at 4000 s. The in-row binding energy E_B^M was set to the 0.18 eV.



Figure 5.5: Simulation snapshot without dimer structures and with instantaneous edge diffusion at 4000 s. The in-row binding energy E_B^M was set to the 0.36 eV.

results presented in the figure 5.3. After the deposition there is a change in the slope, which does not change significantly later on, in the case of low diffusion barriers. Now strong ripening can also occur, as in set (c). However, this strong increase of the mean length continues for the rest of the simulation time. For another set of parameters, set (a) in figure 5.6, the simulation yielded a progression that resembles some aspects of the experiment. After the deposition the mean length rises noticeably in a pace comparable to the experiment and also seems to lead to a regime of saturation. This already indicates that edge diffusion could play a crucial role for the ripening found in the experimental system. A general result of this model is the creation of some extremely large islands as well as many tiny ones. For this reason this model does not agree well with the experiment despite the similar behavior of the mean length.

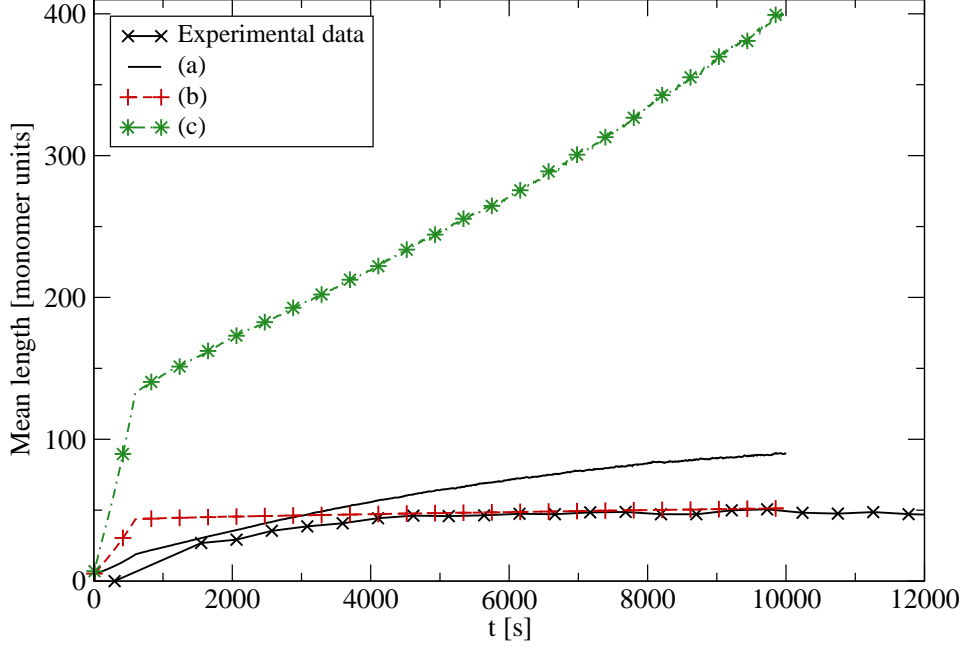


Figure 5.6: Exemplary results of the simulation without dimer structures and instantaneous edge diffusion. The parameters for the best match (a) are: $E_D^1 = 0.50$, $E_D^2 = 0.54$, $E_B^M = 0.2$. For (b) both diffusion barriers are lower ($E_D^1 = 0.44$, $E_D^2 = 0.46$) and the binding energy is higher ($E_B^M = 0.36$). For set (c) the diffusion barriers are lower ($E_D^1 = 0.33$ and $E_D^2 = 0.40$) and the binding energy is higher ($E_B^M = 0.34$).

5.3 Model III

The occurrence of extremely large islands is suppressed in figures 5.7 and 5.8 where the maximum distance a particle can overcome through edge-diffusion is limited by the mean square displacement in the [010] direction for the typical time between jumps perpendicular to the row growth. Similar to the model with instantaneous edge diffusion, the model with the lower binding energy on the left produces longer islands. Thus lower binding energies increase the effect of the edge diffusion. But at the same time the extreme growth of islands is absent also for the smaller binding energy.

The mean length obtained with model III displays a similar behavior to the unlimited case (MIE) and is shown in figure 5.9. The reached mean island sizes are much smaller than in the previous case (see section 5.2). Furthermore there are realizations, which resemble the case without edge diffusion (see section 5.1), where the mean length saturates short after deposition. So this model is capable of producing realizations close to either of the models presented earlier. When the diffusion barriers are very distinct, i.e., the diffusion barrier E_D^2 is much larger than the other, then the limiting distance for the edge diffusion also becomes large, thus resembling the model without a limit. The other case for diffusion barriers very similar in both direction is therefore similar to the model without edge diffusion. Both cases are presented in figure 5.9, set (c) represents a

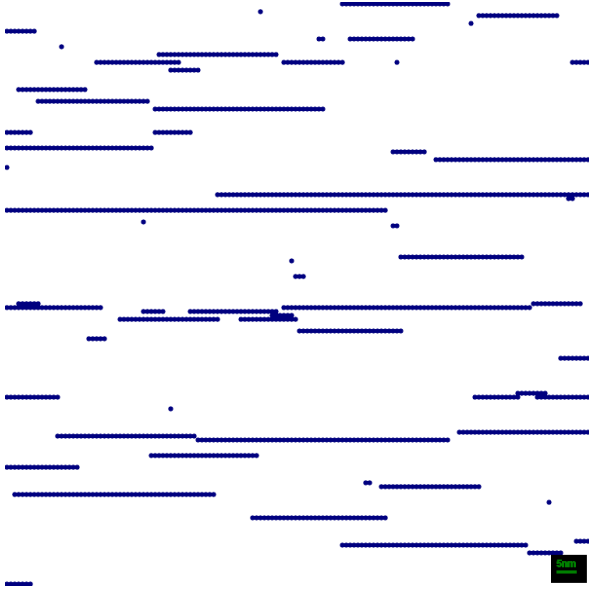


Figure 5.7: Simulation snapshot without dimer structures and with edge diffusion limited by maximum distance at 4000 s. The in-row binding energy E_B^M was set to the 0.18 eV.

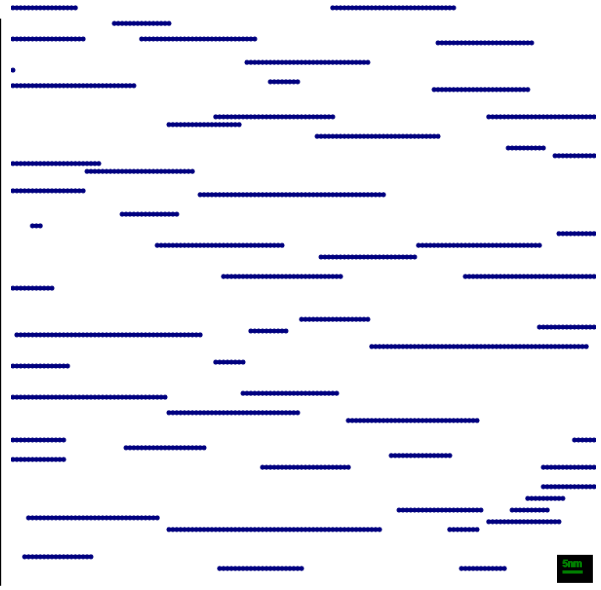


Figure 5.8: Simulation snapshot without dimer structures and with edge diffusion limited by maximum distance at 4000 s. The in-row binding energy E_B^M was set to the 0.36 eV.

realization of a situation close to the model without edge diffusion and set (b) the other extreme with stronger anisotropic diffusion. The anisotropic case shows a very strong ripening after the deposition, which does not saturate within the simulation time. Also similar to the model with instantaneous edge diffusion, this model shows a considerable ripening effect when the diffusion barriers are high, i.e. around 0.5 eV. As an example for that, set (a) in figure 5.9 was included. Simulation results of the mean length show a very distinct ripening and clearly saturate at later times. Unfortunately quantitative agreement could not be achieved.

The different models I-III without dimer structures were not able to produce mean length progressions that agree qualitatively and quantitatively at the same time with the experiment. Even so those models were able to exhibit distinct ripening. This is shown in figure 5.10 for the current model (MLE). As can be seen, the mean length shows well visible ripening and also saturation ($E_B^M = 0.18$ eV). There is an interesting transition from a regime with a binding energy $E_B^M < 0.18$ eV, where no ripening occurs, to ripening that takes place well within the simulated time at intermediate binding energies ($E_B^M = 0.18, 0.2$ eV). As the binding energy increases further the ripening effect decreases and the curves become more and more flat ($E_B^M > 0.2$ eV). In order to check if the observed ripening is responsible for the experimentally measured patterns, the island size distributions for the simulation of figure 5.10 were collected. Those distributions are shown in figures 5.11-5.14. The curves that show ripening similar to the experimental case are those with the intermediate binding energies 0.18 and 0.20 eV. Their

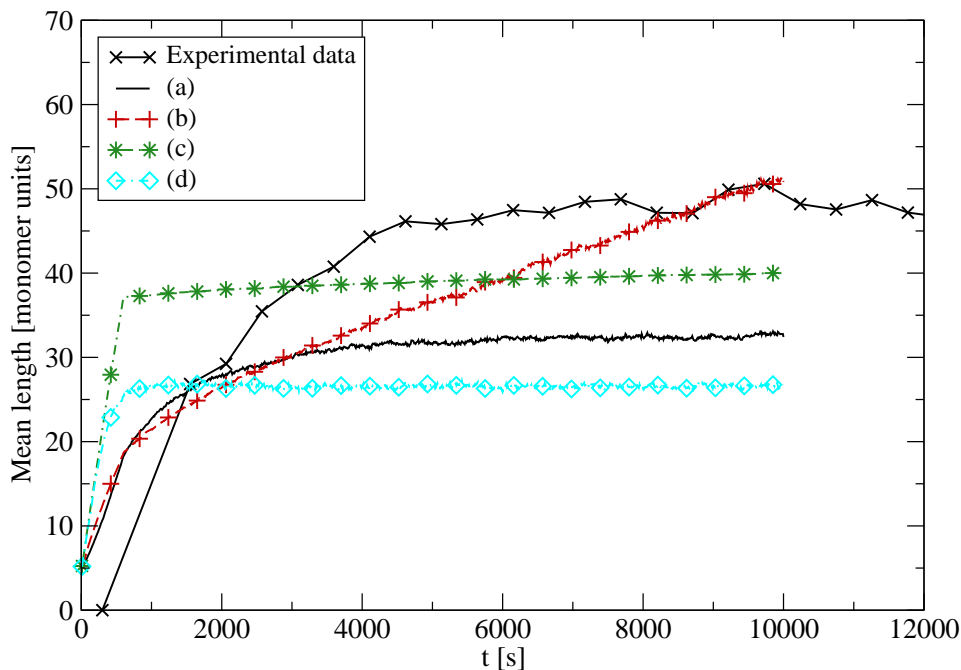


Figure 5.9: Exemplary results of the model without dimer structures and the implementation of the edge diffusion mechanism limited by maximum distance. The parameters for the best match (a) are: $E_D^1 = 0.50$, $E_D^2 = 0.54$, $E_B^M = 0.18$. For (b) the diffusion anisotropy is higher ($E_D^1 = 0.40$ and $E_D^2 = 0.60$). For set (c) the binding energy is higher ($E_B^M = 0.36$) and in set (d) the diffusion barriers are lower ($E_D^1 = 0.44$ and $E_D^2 = 0.46$).

island size distributions differ strongly from those experimentally observed, especially the distributions where the ripening ceases during the simulation (see figure 5.12). This is emphasized again later in figures 5.15 and 5.16. Despite the different implementations of the edge diffusion all models (I-III) without dimer structures⁸ showed this transition concerning the ripening of the mean length and also their respective island size distributions are similar to the presented case of edge diffusion limited by maximum distance.

The figures 5.15 and 5.16 show the island size distributions for the models II-III (without dimer structures) with parameters, which produced the best agreement with the experimental data. Because of the rather poor agreement between the model I (without edge diffusion) and the experiment, no length distribution is displayed for that case. But even for the other model systems II and III the agreement of the size distributions is rather poor, even though the mean length of these models produced similar features.

⁸This includes the model without edge diffusion as well.

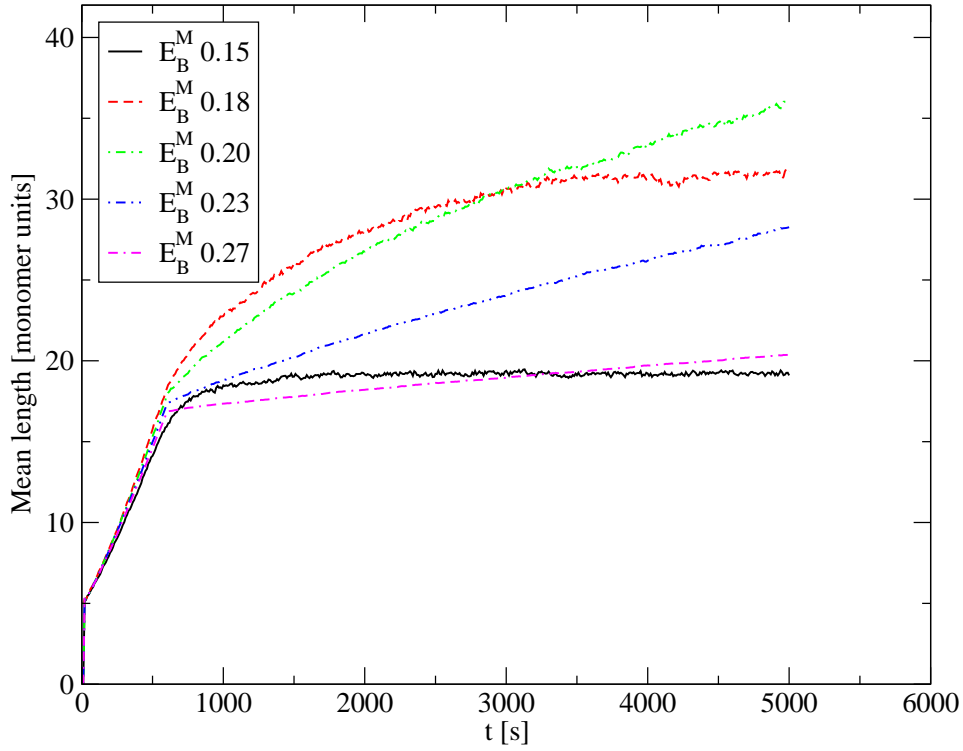


Figure 5.10: Observed ripening in the model without dimer structures and edge diffusion limited by maximum distance. The diffusion barriers are $E_D^1 = 0.5$ eV in the direction of row growth and $E_D^2 = 0.54$ eV otherwise.

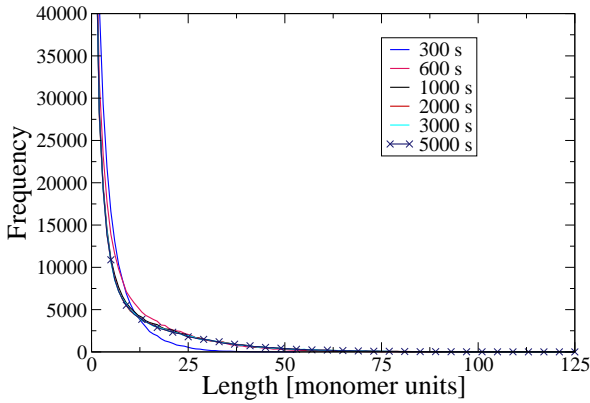


Figure 5.11: Length distributions for the mean length progression with in-row binding energy of $E_B^M = 0.15$ eV, where no ripening occurs.

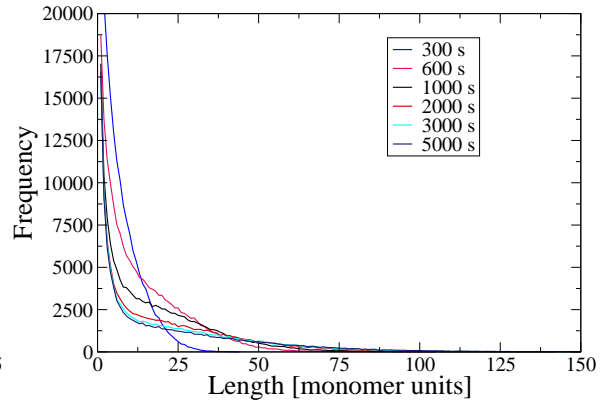


Figure 5.12: Length distributions for the mean length progression with in-row binding energy of $E_B^M = 0.18$ eV, where ripening is observable and saturates within the simulation time.

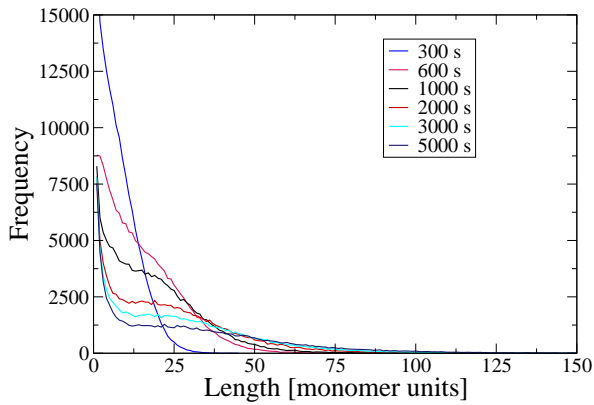


Figure 5.13: Length distributions for the mean length progression with in-row binding energy of $E_B^M = 0.20$ eV, where ripening is observable but does not saturate during the simulation.

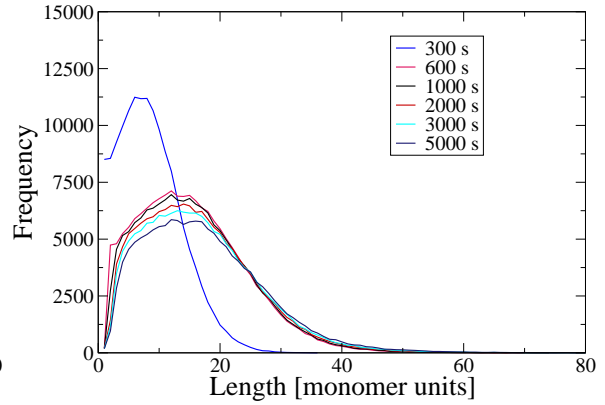


Figure 5.14: Length distributions for the mean length progression with in-row binding energy of $E_B^M = 0.30$ eV, where ripening is slowed down due to the high binding energy.

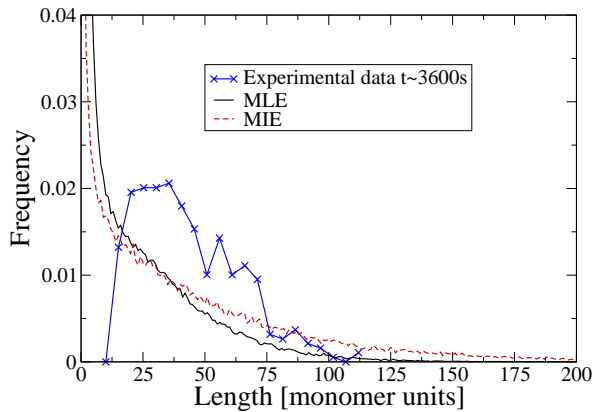


Figure 5.15: Length histograms of the simulations without dimer structures roughly one hour after the deposition along with the corresponding histogram from the experiment. The diffusion ratios for both simulation sets are $E_D^1 = 0.50$ and $E_D^2 = 0.54$. The binding energy for model MIE is $E_B^M = 0.20$ and for the other (MLE) $E_B^M = 0.18$.

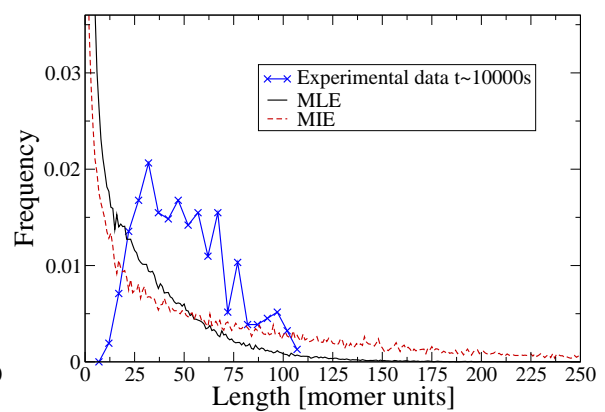


Figure 5.16: Length histograms of the simulations without dimer structures roughly 160 minutes after the deposition along with the corresponding histogram from the experiment.

5.4 Model IV

In the following the snapshots for the models that incorporate dimer structures are presented. Figures 5.17 and 5.18 show snapshots from the model without edge diffusion also one hour and 160 minutes after the deposition, respectively. Note that the color blue (dark gray, round) marks monomer particles and magenta (light gray, straight) dimer particles.

There are clearly differences between those two times. In the earlier snapshot many monomer rows and particles are apparent, which are nearly gone in the right figure leaving mainly dimer structures visible. As in the simulation without dimer structures the islands are rather small and do not seem to grow considerably after the first picture.

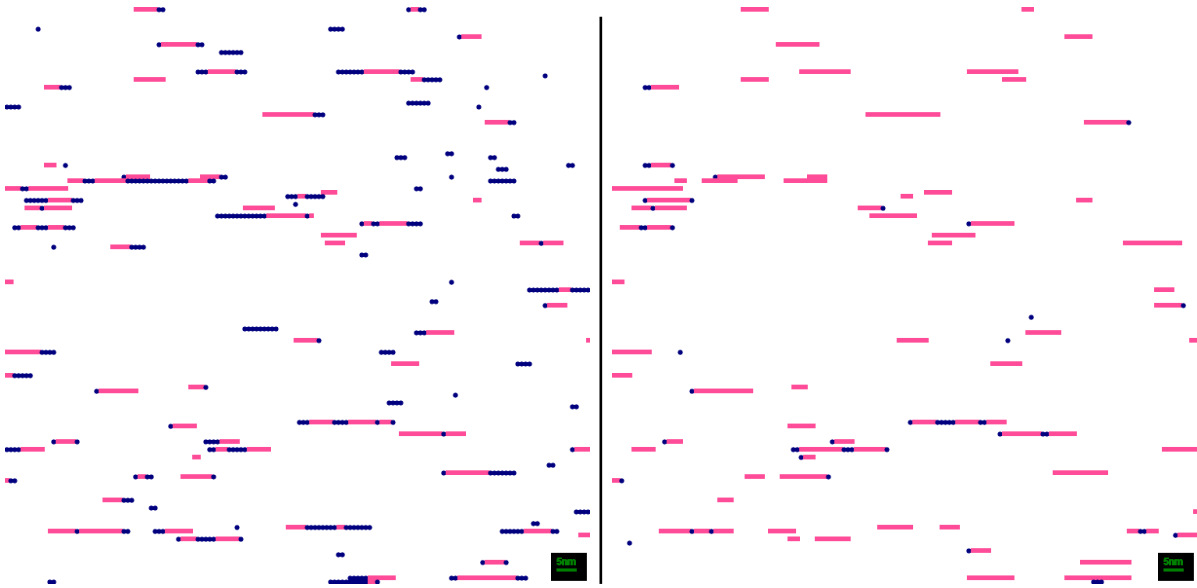


Figure 5.17: Simulation snapshot with no edge diffusion at 4000s, i.e. one hour after the deposition was finished.

Figure 5.18: Simulation snapshot with no edge diffusion at 10000s, i.e. during the saturation regime.

Model IV does not exhibit a strong ripening regime after the deposition as shown in figure 5.19. In addition the mean lengths achieved with this model are rather small. But there is another feature that could be observed in this particular model. When the ratio of dimer particles saturates the mean length of the islands increases noticeably and slightly decreases afterward as shown in figure 5.19. In most of the shown cases the mean length is slightly larger when the mean length saturates again and remains nearly constant for the rest of the simulation. This was not observed in the model without dimer structures, therefore solely the introduction of those structures must be responsible for this feature. In order to find the reason for this increase in the mean length, island distributions around this feature were extracted for different row species. This is shown in figure 5.20, which shows the distribution of any row type (monomers, dimers

and the mixture of both), and figure 5.21, which shows the contribution of dimers to the island size distribution, those distributions belong to the blue curve of figure 5.19 ($E_{\text{Barrier}} = 1.21$). The contribution missing to the peak in the full island size distribution in figure 5.20 is caused by mixed rows (compare with figure 5.17). In the shown case this effect occurs quite after the deposition was finished but when only a few dimers are present and the monomers have a monotonically decreasing distribution. Shortly after that, when the mean length begins to rise, the distribution of the monomers collapses. This is responsible for the minimum which develops in the distribution in figure 5.20. At the same time the distribution of dimer islands grows. So all small monomer islands vanish and lead to the increase of the dimer size distribution. Then the monomer distribution shrinks further but does not vanish⁹. The reason for the lower ratio of dimerised particles¹⁰ is the existence of mixed rows, where dimer-type and monomer-type rows are alternating, this is well visible in figure 5.17. These rows are more stable than pure monomer rows because particles that are enclosed between dimer-type particles can only escape in the direction with the higher diffusion barrier. The size distributions of mixed and pure dimer islands are quite similar in terms of form and magnitude at the later times.

In summary the different row types contribute as follows to the full island size distribution: The very left flank is only due to the monomer islands, which shrinks considerably over time, to the following peak the pure dimer islands and the mixed islands contribute, as mentioned quite evenly at later times ($t > 5\,500\text{s}$) and before that¹¹ the mixed islands dominate this peak.

⁹Not shown in figure 5.20, but in figure 5.19 the ratio of dimers never approaches one.

¹⁰as compared to the other models with a similar set of parameters.

¹¹before the maximum dimer ratio is reached.

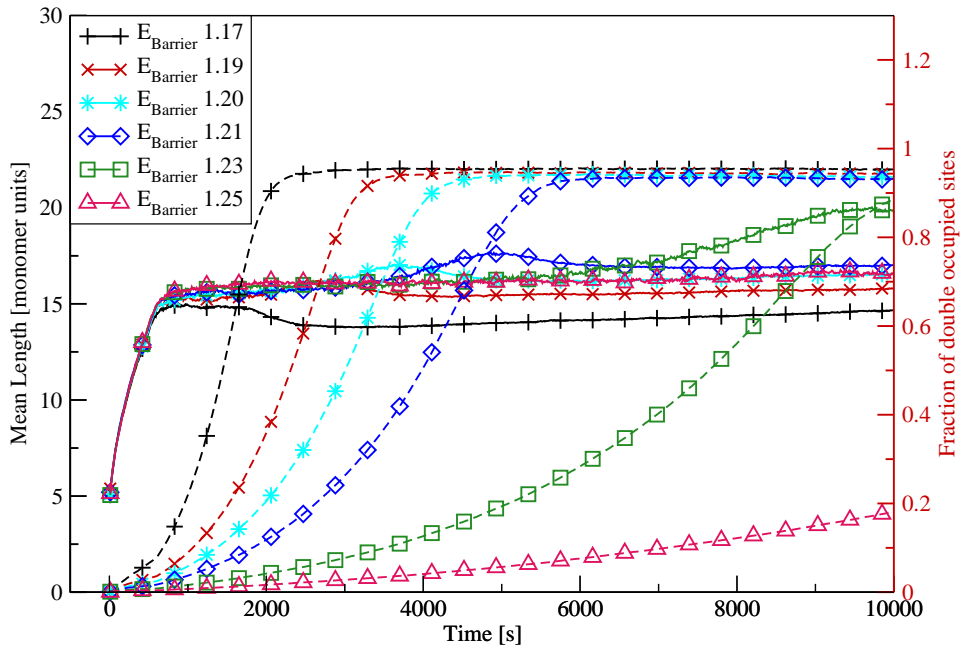


Figure 5.19: Combined plots of the mean length and the ratio of dimer particles for the model with dimer particles but without edge diffusion.

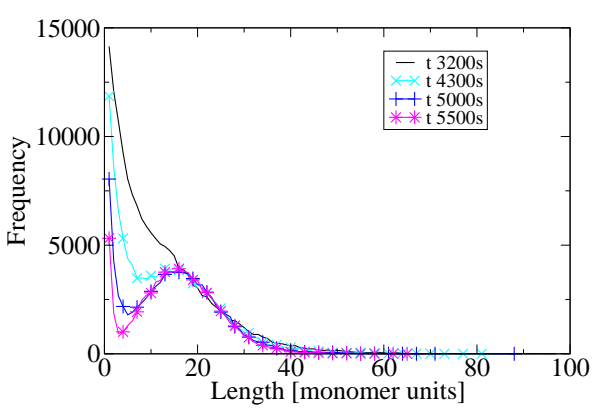


Figure 5.20: Island size distributions for the observed feature in the mean length development of the model considering dimer structures but without edge diffusion for rows consisting of monomers and dimers.

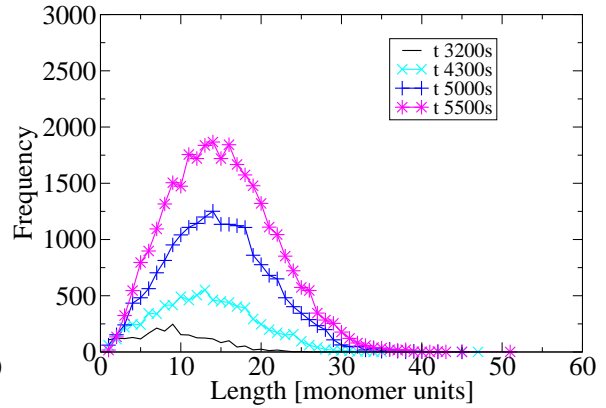


Figure 5.21: Like the left pictures, this time the island size distribution for the dimer rows is shown.

5.5 Model V

The model considered here is with the conventional edge diffusion mechanism (DCE). In figure 5.22 one hour after the deposition almost all of the edge diffusing particles found their way to a row end. Compared to the model without edge diffusion the ratio of monomer particles is remarkably lower. In figure 5.23 the vast majority of particles are dimerised and even the edge diffusing particles are vanished completely. This could be an indication that dimerisation is dominated through the edge diffusion mechanism, where the dimer creation barrier E_{Barrier} does not apply.



Figure 5.22: Simulation snapshot with conventional edge diffusion at 4000s, i.e. one hour after the deposition after the deposition was finished. The green color indicates edge-diffusing particles.

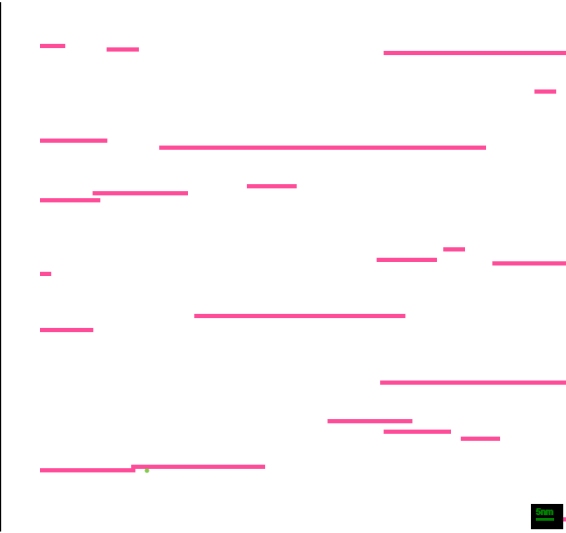


Figure 5.23: Simulation snapshot with conventional edge diffusion at 10 000 s, i.e. during the saturation regime. Green color indicates edge-diffusing particles.

Figure 5.24 shows the mean length progression of this model for some parameter sets and in figure 5.25 the corresponding fractions of dimer particles are shown. This model produces very distinct ripening and saturation regimes, sets (a) and (d) in figure 5.24 are good examples for that. But it is also possible to suppress the ripening regime right after the deposition or to shorten it and to minimize the effect. This can be seen in sets (b) and (c). The corresponding dimer ratios, as displayed in figure 5.25, support the notion that the strong ripening ends when this ratio reaches one. In the case of set (c) no strong ripening was observed, because the fraction of dimers reached one shortly after the deposition. But with a slightly lower dimer fraction, the ripening after the deposition becomes well visible, as in the cases of set (a) and (c). For more slowly increasing ratios of dimers the effect is enhanced. From the displayed simulation results the set (a) shows good agreement. The rapidly growing ratio of dimers also fits well to the experimental observations of very few monomer rows one hour after the deposition.

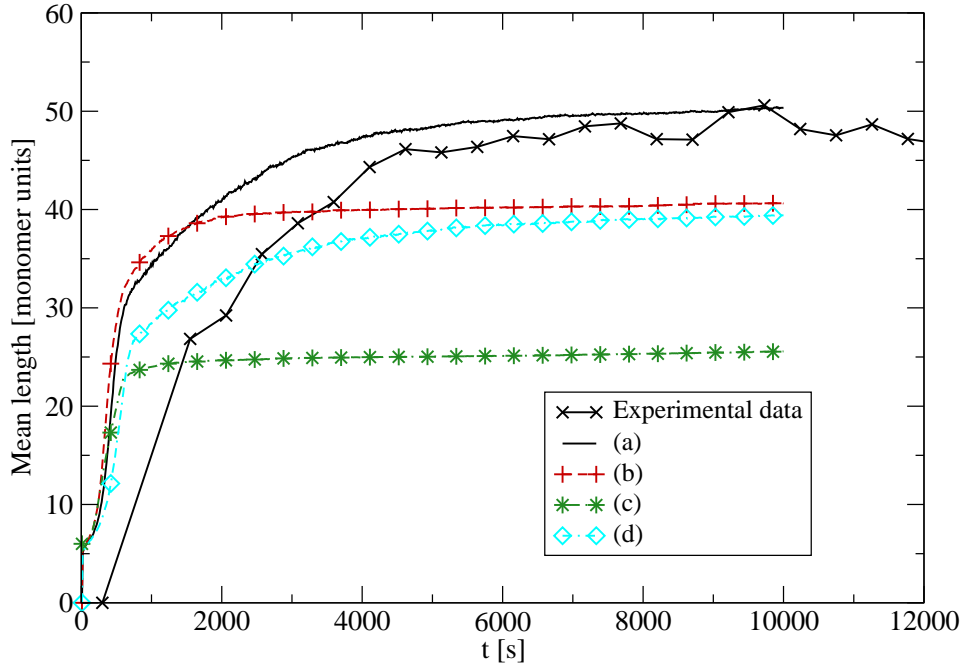


Figure 5.24: Mean length of some chosen examples for the model with the conventional edge diffusion mechanism. The parameters for the best match (a) are: $E_D^1 = 0.475$, $E_D^2 = 0.49$, $E_B^M = 0.15$, $E_{\text{Barrier}} = 1.21$, $E_{\text{Edge}} = 0.50$, $E_{\text{Dimer}} = 0.50$ and $DR = 1000$. For set (b) and (c) the dimerisation is faster, i.e. $E_{\text{Barrier}} = 1.2$ and $E_{\text{Barrier}} = 1.1$ eV, respectively. For set (d) the diffusion barriers are higher ($E_D^1 = 0.49$ and $E_D^2 = 0.5$ eV).

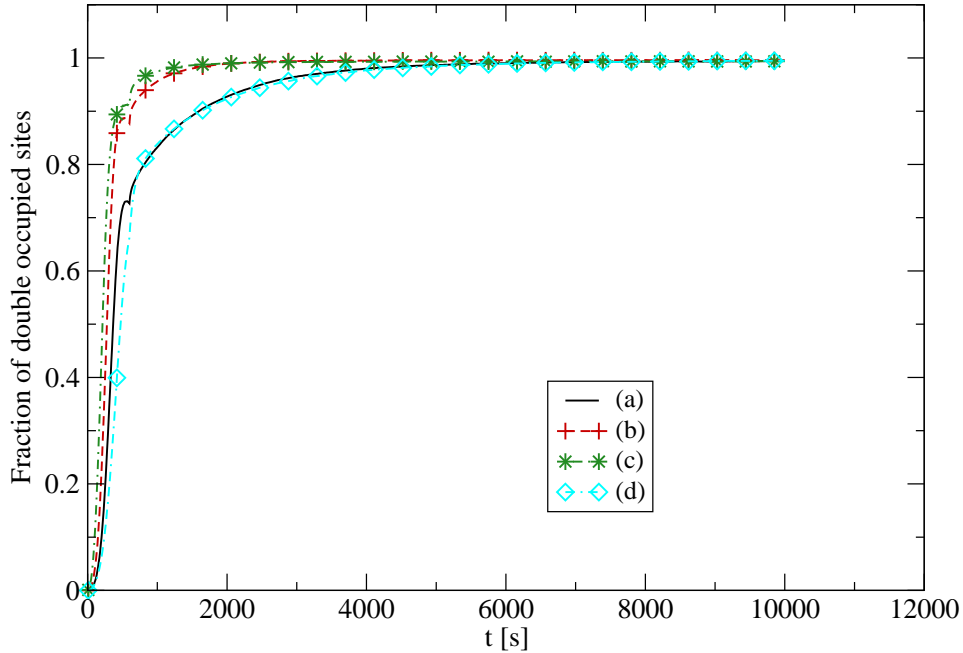


Figure 5.25: The ratio of dimers corresponding to the data in figure 5.24.

5.6 Model VI

In figures 5.26 and 5.27 snapshots for the model with instantaneous edge diffusion are presented at 66 and 166 minute simulation time, respectively. As in the model IV (D) one hour after the deposition, rows of monomer type are visible and their amount is considerable. Similar to model V (DCE), there are no more visible monomer particles at the later time. Already in those snapshots the rather long islands are striking.

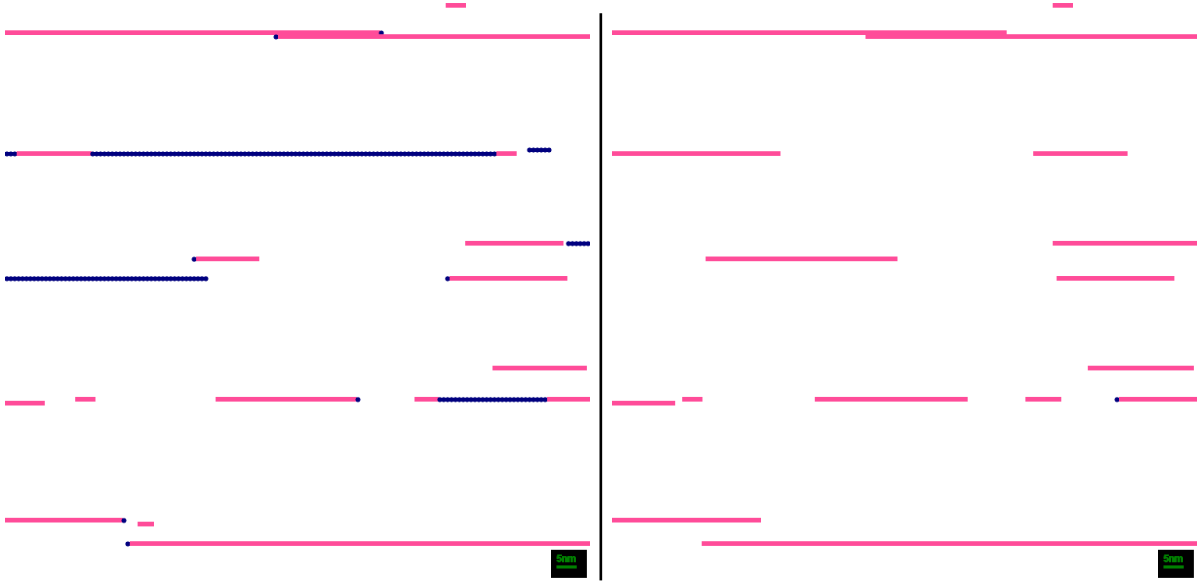


Figure 5.26: Simulation snapshot with instantaneous edge diffusion at 4000 s, i.e. one hour after the deposition after the deposition was finished.

Figure 5.27: Simulation snapshot with instantaneous edge diffusion at 10000s, i.e. during the saturation regime.

Figure 5.28 shows some results of the mean length for this model system. As in the case of no dimer structures this model can produce extremely large islands, even for rather high diffusion barriers. As an example for that case set (b) in figure 5.28 was included. This simulation shows a very clear saturation with a nearly constant mean length after 66 minutes as well as a very pronounced ripening regime. There is a shoulder right after the deposition, after which the mean length starts to grow more and more strongly until a constant slope is reached and the mean length saturates. Such a distinctive feature was not observed experimentally. Another interesting case is presented in set (c). Here the in-row binding energy is slightly higher and the energy barrier for the dimer creation is lower than in the case of the set (b). Now the mean length does not rise considerably after the deposition, but decreases slightly and remains then constant. Set (d) in contrast is similar to set (b), but with an extended region of very slow growth of the mean length. The reason for the delay is the slower dimerisation rate. In terms of the mean length progression, set (a) agrees very well with the experiment.

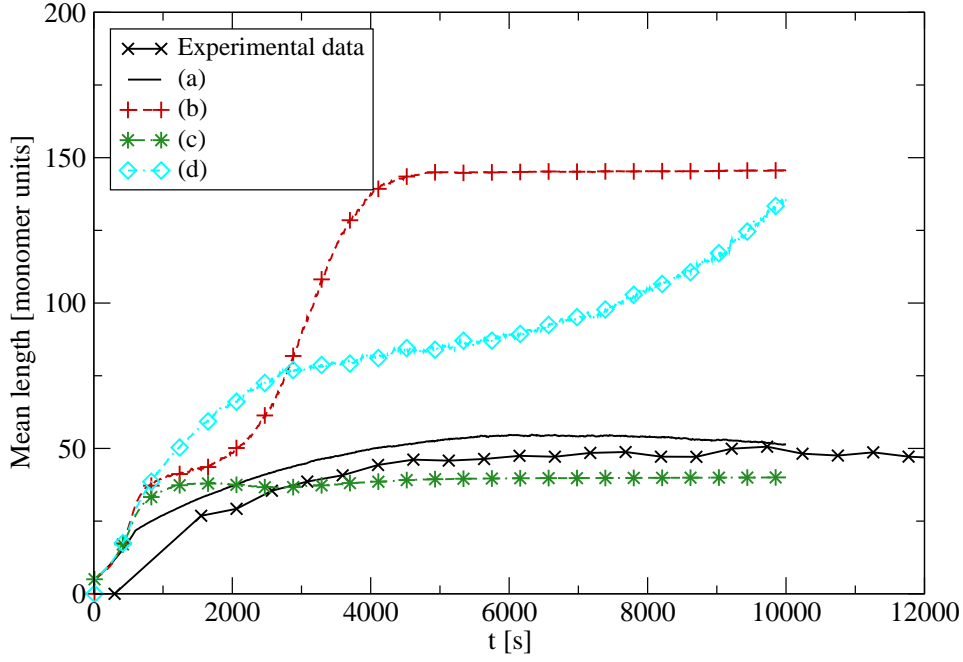


Figure 5.28: Exemplary results of the model system incorporating dimer structures with instantaneous edge diffusion. The parameters for the best match (a) are: $E_B^M = 0.20$, $E_{\text{Barrier}} = 1.20$, $E_{\text{Dimer}} = 0.54$, $E_D^1 = 0.50$, $E_D^2 = 0.51$ and $\text{DR} = 1000$. For sets (b) and (c) the binding energy E_B^M is smaller (0.14, 0.16 eV) and in set (c) the dimerisation was faster ($E_{\text{Barrier}} = 1.16$ eV). In set (d) the dimerisation is comparable to set (a).

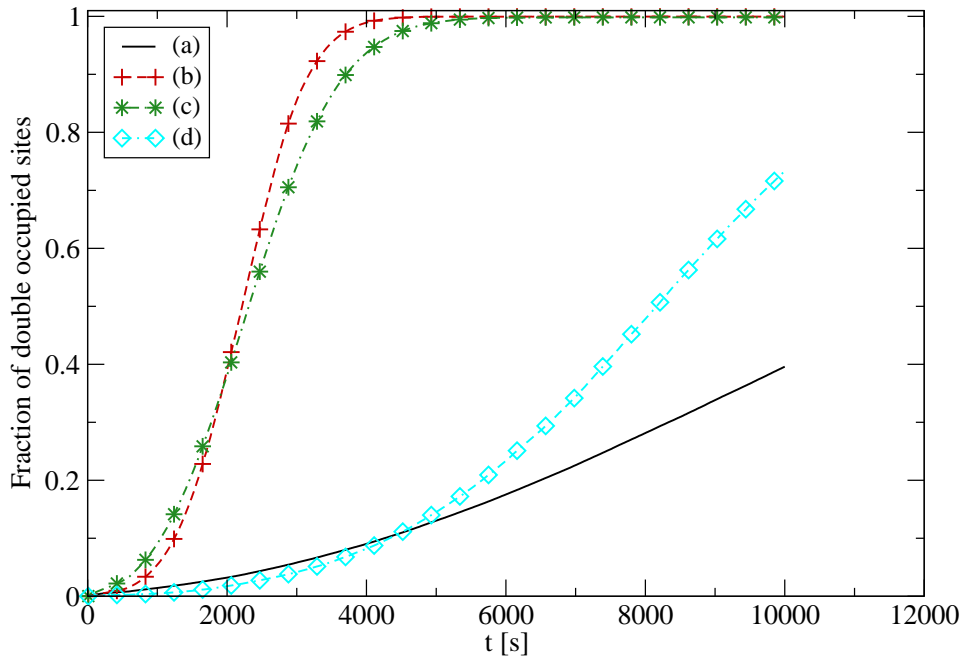


Figure 5.29: Fraction of dimerised species of the total coverage corresponding to the mean length curves of figure 5.28.

The ratios of dimerised particles corresponding to the mean lengths in figure 5.28 are shown in figure 5.29. From the comparison of both figures one can see that the region with the strong increase of the mean length for set (b) and (d) coincides with high ratios of dimerised particles. Furthermore the saturation of the mean length occurs when almost all particles are dimerised. Thus the saturation regime resembles the progression of the mean length behavior in the models without dimer structures when the in-row binding energy is large (compare figure 5.3 and 5.6). The other simulation data presented in figure 5.29, set (a), is very close to the experiment. Despite a seeming agreement in mean length, the dimerisation is very low at the end of the simulation time. Additionally the mean length decreases slightly at the end¹², which would be unlikely to happen in the experimental system.

¹²For a longer simulation conducted with the same set of parameters, it was found that the mean length decreases even more afterward.

5.7 Model VII

As before the picture on the left side was taken one hour after the deposition (figure 5.30) and diagram 5.31 was taken roughly 160 minutes after the deposition. At first glance the amount of monomer particles seems lower than in the implementations without edge diffusion and instantaneous edge diffusion but higher compared to the conventional edge diffusion mechanism. As observed before at the later time almost all monomer particles have vanished and only dimerised rows are visible. The length of the simulated rows lies between the lengths of the instantaneous edge diffusion implementation and the results of the other models.



Figure 5.30: Simulation snapshot with edge diffusion limited by maximum distance at 4000s, i.e. one hour after the deposition was finished.



Figure 5.31: Simulation snapshot with edge diffusion limited by maximum distance at 10 000 s, i.e. during the saturation regime.

Figures 5.32 and 5.33 present the mean length and the ratio of dimer particles of this model. As before the different regimes can be strongly pronounced for certain parameter sets. As an example for such a curve, set (a) was chosen, which matches well with the experimental data. Also for this model the mean length saturates when the fraction of dimers approaches one. The mean length of sets (b) and (c), however, seems not to fit with this notion, because the mean length does not rise considerably before, but as the fraction of dimers reaches one the fluctuations in the mean length cease. The data presented in set (d) in the plot reaches full dimerisation shortly after the deposition, so there is no noticeable increase in the mean length afterward.

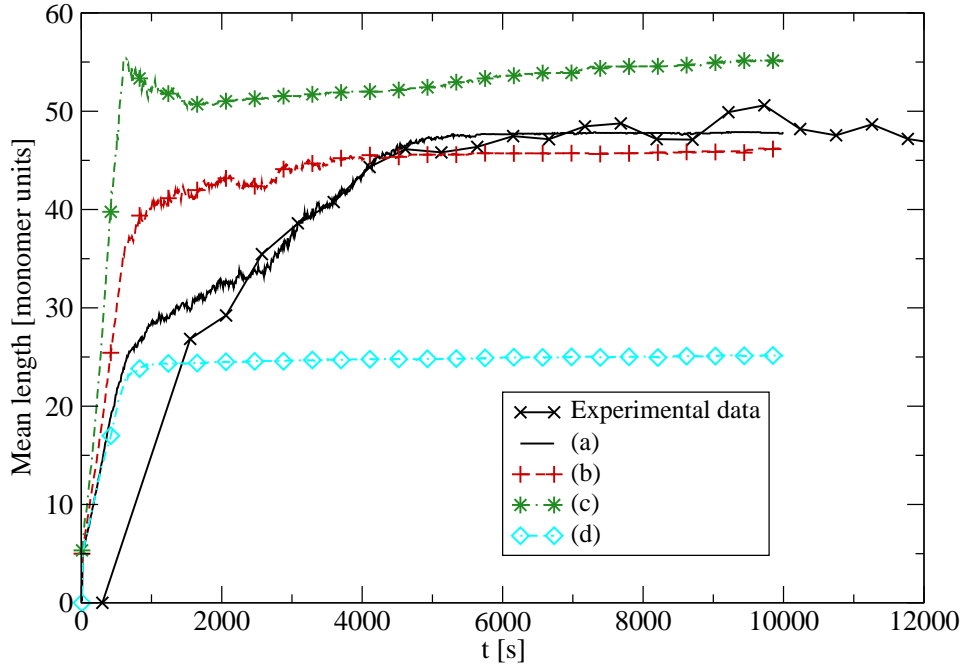


Figure 5.32: Some results of the simulation with dimer structures and edge diffusion limited by maximum distance. The parameters for the best match (a) are: $E_D^1 = 0.48$, $E_D^2 = 0.49$, $E_B^M = 0.18$, $E_{\text{Barrier}} = 1.20$, $E_{\text{Dimer}} = 0.54$ and $\text{DR} = 1000$. For set (b) the diffusion anisotropy is higher ($E_D^1 = 0.44$, $E_D^2 = 0.48$ eV). In set (c) the binding energy E_B^M is lower (0.16 eV) but dimerisation is faster ($E_{\text{Barrier}} = 1.1$ eV). For set (d) the diffusion barriers are lower ($E_D^1 = 0.40$, E_D^2 eV).

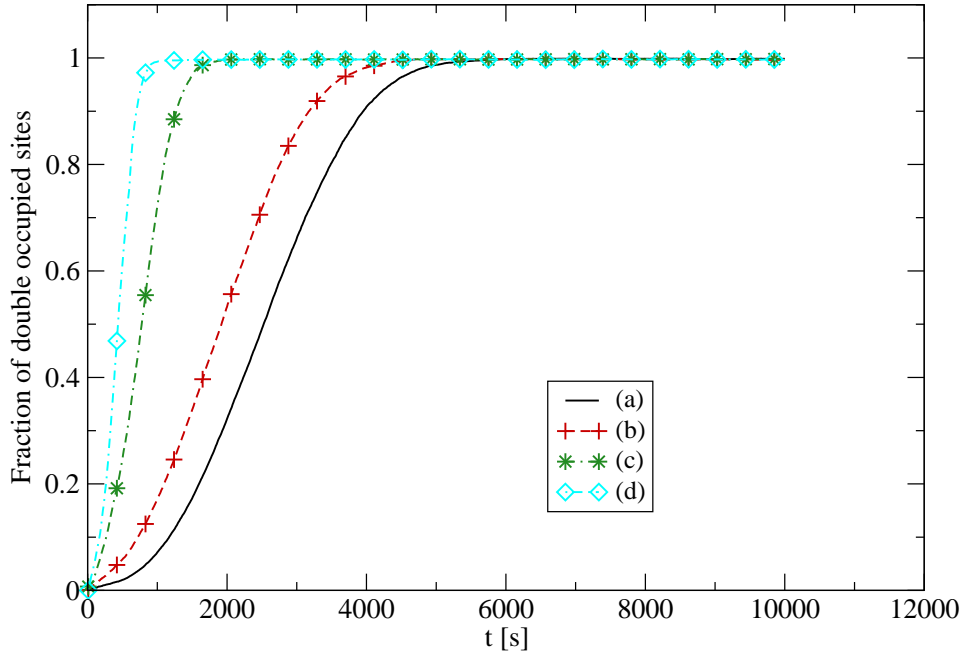


Figure 5.33: To figure 5.32 belonging fraction of dimers.

5.8 Model comparison

In summary all the models presented in sections 5.1-5.7 show the formation of one-dimensional structures. The amount of monomer particles found at a certain time differ from model to model and the intensity of the ripening varies. The introduction of dimer-like particles does not change the occurrence of one-dimensional islands but does make the snapshots look less dense due to the fact that after full dimerisation only half as many of the originally deposited particles occupy the surface. From investigating the morphologies alone no sufficient information about the kinetics is available, so that it is not possible to evaluate which model recreates the experimental kinetics. For that reason the ripening behavior as well as the length distributions are utilized.

In general the models I-III considering only monomers all yield one-dimensional structures, which grow along the direction associated with a binding energy. As shown previously (see sections 5.1-5.3), models I-III do not recreate the experimental data well. The achieved mean lengths are smaller than in the experiment, especially when the two different ripening regimes were observable. In those cases the corresponding island size distributions are different to the experimental ones as well. In contrast the models including dimers (models V-VII) produced reasonably similar island size distribution as presented in figures 5.34 and 5.35 in addition to the good agreement of the mean length behavior as shown previously (see sections 5.5-5.7). The agreement is good for the model with edge diffusion limited by a maximum distance (DLE) and the conventional edge diffusion mechanism (DCE). The system with the instantaneous edge diffusion (DIE), however, shows completely different progress of a monotonically decreasing distribution¹³, whereas the other two models produce a well defined maximum or at least a shoulder for either of the shown times. In fact for the later time the distributions of those models are nearly identical. The differences to the experimental distribution are located at smaller lengths, but the tails of the ISD's are in good agreement. The additionally shown contributions of the dimer rows in the insets of figures 5.34 and 5.35 agree well in terms of form and peak position with the experimental measured progressions and are also nearly identical at the later time. For the model with instantaneous edge diffusion (DIE) the island length distribution deviates in several aspects from the experimental one. Islands as large as that were not observed experimentally, indicating that this approximation for edge diffusion over estimates the capability of the actual helicene particles. Additionally the region of small islands is pronounced more strongly and the overall progression mainly stays monotonically decreasing.

The plots presented in the following will show the ripening of the mean length and the temporal development of the ratio of dimers to monomers as well as histograms for selected times at a fixed set of parameters. The parameters used are summarized in table 5.1. The set of parameters was chosen so that one of the most promising models, the model with limited edge diffusion (DLE), would fit best to the experiment. All other models were then run with this parameter set in order to facilitate a comparison of the

¹³except for a small dip at very small lengths.

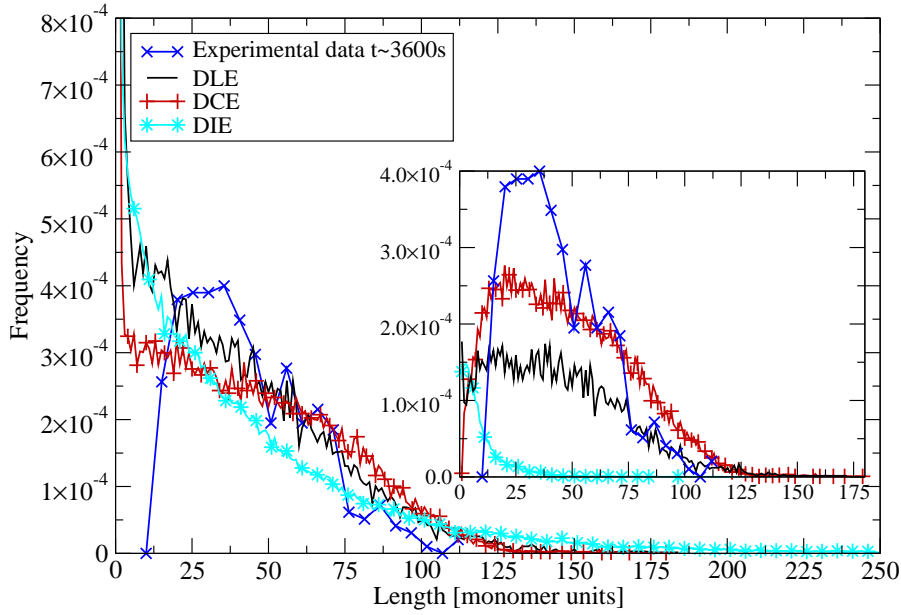


Figure 5.34: Comparison of the island size distributions of the models considering dimer structures for parameters sets reproducing the experimental mean length behavior well. The data was taken roughly one hour after the deposition. The inset shows the contribution of dimerised rows to the whole length distribution. The parameters for the shown sets are: $E_D^1 = 0.48$, $E_D^2 = 0.49$, $E_B^M = 0.18$, $E_{\text{Barrier}} = 1.20$, $E_{\text{Dimer}} = 0.54$ for the model DLE; $E_D^1 = 0.475$, $E_D^2 = 0.49$, $E_B^M = 0.15$, $E_{\text{Edge}} = 0.50$, $E_{\text{Barrier}} = 1.21$, $E_{\text{Dimer}} = 0.50$ for model DCE and $E_D^1 = 0.50$, $E_D^2 = 0.51$, $E_B^M = 0.20$, $E_{\text{Barrier}} = 1.20$, $E_{\text{Dimer}} = 0.54$ for the other simulation (DIE).

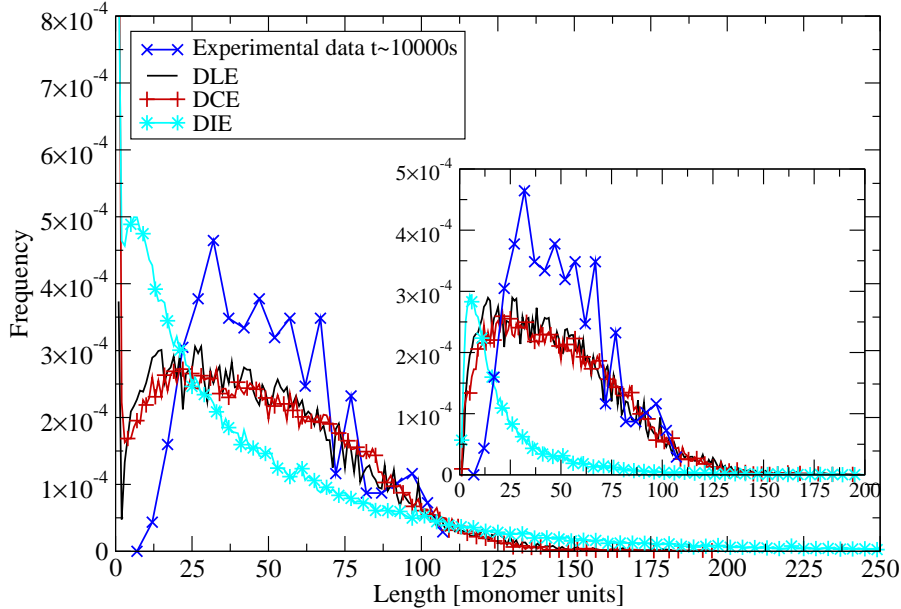


Figure 5.35: Comparison of the island size distributions of the models considering dimer structures for parameters sets reproducing the experimental mean length behavior well. The data taken roughly 160 minutes after the deposition. The inset shows the dimer contribution to the whole island size distribution.

Symbol	Value
ν	$10^{10} \frac{1}{s}$
E_D^1	0.48eV
E_D^2	0.49eV
E_D^3	0.558eV
E_D^4	0.568eV
E_B^M	0.18eV
E_B^D	0.36eV
E_{Barrier}	1.2eV
E_{Dimer}	0.6eV
DR	1 000
Θ	6%
M	2048

Table 5.1: Set of the parameters used in the KMC simulations.

different models. This is especially important to distinguish the influence of the edge diffusion mechanisms. For those figures the simulation data of several runs (five and more) was used to calculate a mean value and the standard deviation.

As before the models I-III concerning only monomer type particles are discussed first. In figure 5.36 the mean length data of all models without dimer structures are shown as well as the experiment. None of the models follows the experimental curve. Most models yield a too small mean length, with the smallest islands found in the simulations without edge diffusion (M). As already suspected the simulation without edge diffusion yields larger islands with increased in-row binding energy. Another remarkable feature is that the increase of the mean length stops right after the deposition is switched off. So there is essentially no post-deposition ripening for this set of parameters, which is in contradiction to the experimental system. The simulations with edge diffusion limited by maximum distance (MLE), however, show no strong dependence on the in-row binding energy concerning the value of the mean length at later times. This time the simulation with the lesser binding energy yields slightly larger islands and also has a rather smooth transition after the deposition. A considerable ripening regime is also absent from this model. The most outstanding behavior is found for the simulation with instantaneous edge diffusion (MIE). The difference between the two shown in-row binding energies is very large compared to the other models in figure 5.36. Like the other implemented edge diffusion mechanisms the simulation with the lesser binding energy yields the larger islands. While the simulation with the larger energy lies below the experimentally observed mean length the other one produces extremely large islands. Another significant difference of this model is that now the simulation with the lower energy shows a distinct ripening behavior after the deposition. Compared to the experimental curve the ripening regime of this simulation is rather shallow. Even after that distinct strong ripening

regime the mean length continues to grow, which is not observable in the other models nor in the experiment. Furthermore after 6 000 s the mean length starts to grow stronger again and contradicts the experimental data even more. The cause for this unexpected property might be the formation of extremely large islands in this model, so that finite size effects are likely to occur and may be responsible for this increase at later times.

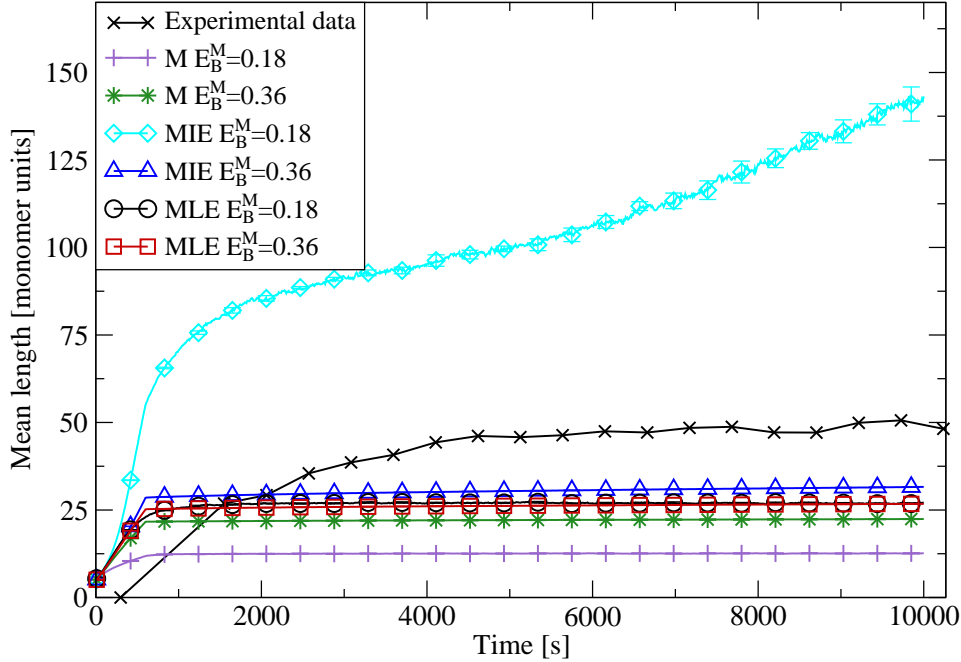


Figure 5.36: Comparison of the ripening of the mean length for the various models without dimer structures (model I-III).

The figures 5.37 and 5.38 show the length histograms of the models considering only monomer structures along with the experimental measured length distribution for one hour and 160 minutes after the deposition, respectively. The best agreement is achieved for the simulations with the higher in-row binding energies. In this case all models show a very similar form of the length distribution in figure 5.37. In general the distributions are too shallow and the maximum is at a length too small. The models with the smaller binding energy show all a monotonically decrease, which does not match with the experimental curve. A similar behavior can be observed in figure 5.38, where the histograms 160 minutes after the deposition are shown.

After the models with only one particle type, the mean length of the different models IV-VII with dimer structures are presented. Additionally to the mean length data the ratio of dimerised particles will be shown. In figure 5.39 the mean length of the different simulations is shown together with the experiment. In contrast to the models I-III the mean length does not vary so strongly but differences between the various edge diffusion implementations are clearly visible. The smallest islands are again found in the simula-

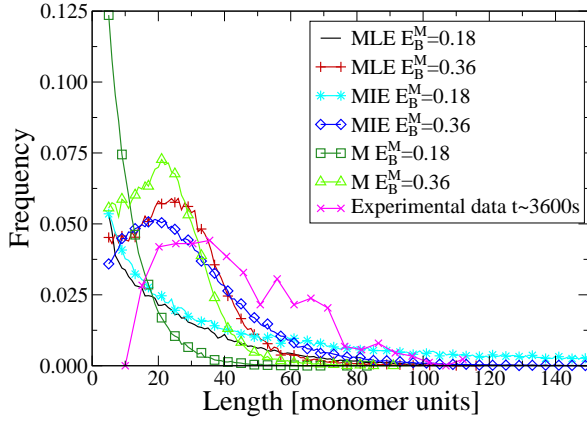


Figure 5.37: Comparison of the length histograms of the models without dimer structures and the experimental data around one hour after the deposition. Monomer as well as dimer islands are included.

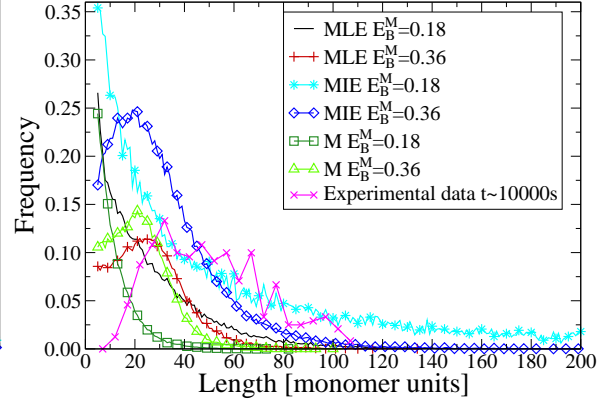


Figure 5.38: Comparison of the length histograms for monomer and dimer rows of the models without dimer structures and the experimental data at around 160 minutes after the deposition.

tion which omits edge diffusion. Slightly larger rows are produced by the algorithm that implements the conventional edge diffusion mechanism. And also, like in the case of no dimer structures, the instantaneous edge diffusion algorithm yields the largest mean length. This time the mean length is more moderate and not much larger than in the simulation with the edge diffusion limited by maximum distance. Besides the differences in the mean length achieved during the saturation regime (well past 5 000 s), there are differences in the progression.

The model D with no edge diffusion reveals no regime of ripening; after the deposition the mean length stays constant and decreases slightly around 6 000 s. The simulation with the conventional edge diffusion (DCE) shows a similar progress with a higher mean length and no decrease. The other two simulations (DIE, DLE) yield very interesting and distinct progressions for the mean length. The model with the limited edge diffusion mechanism (DLE) shows a considerable slope after the deposition. After this regime the mean length saturates and stays constant, which also coincides with the experimental observations. The model VI with instantaneous edge diffusion, however, shows a very strong increase in the mean length after the deposition stops. It reaches a peak at around 2 000 s, then decreases slightly and finally saturates at 5 000 s. This behavior clearly contradicts the experimental observations.

The agreement between the model with the limited (DLE) and the conventional (DCE)¹⁴ edge diffusion and the experiment, however, is *excellent*. The strong ripening after the deposition is well reproduced. Its absence or different behavior, respectively, in the other models (DIE and D) leads to the conclusion that these edge diffusion implementations

¹⁴As shown in section 5.5 in figure 5.24.

are not suitable to cover the processes, which are essential in the experiment. The model DCE can produce ripening behaviors similar to the model with edge diffusion limited by maximum distance at a slightly different parameter set as shown in section 5.5. The development of the ratio of dimer particles is presented in figure 5.40. As

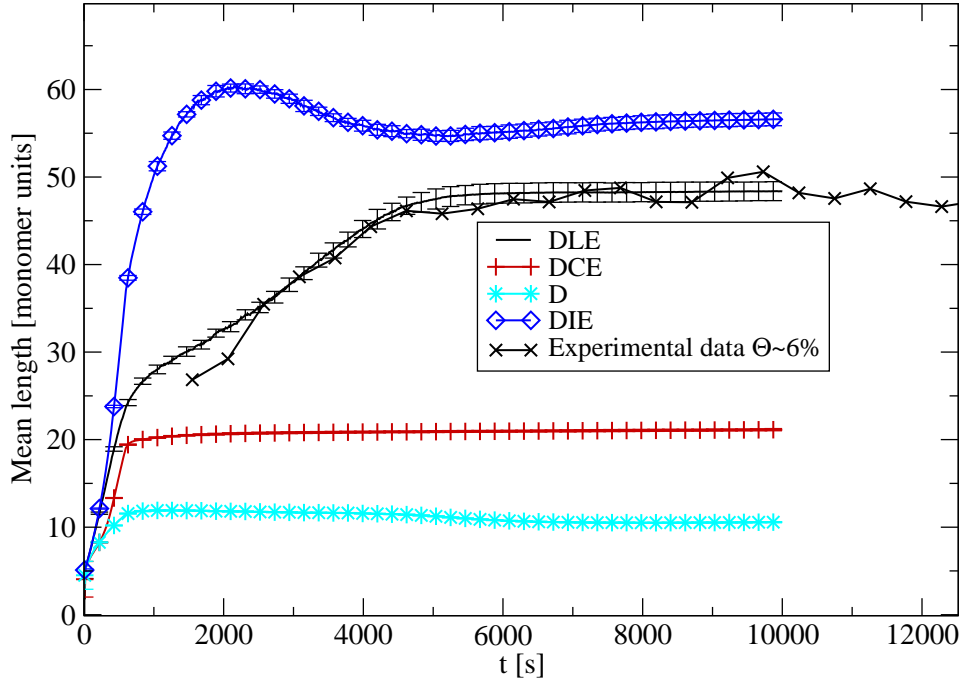


Figure 5.39: Comparison of the ripening of the mean length for the various models which take dimer structures into account.

expected the simulation with no edge diffusion has the weakest increase of dimer particles. Furthermore the ratio does not reach one, i.e. a value well below. The model with instantaneous edge diffusion (DIE) has a higher slope of the dimer fraction and reaches nearly one as the end of the simulation time is approached. The model with limited edge diffusion (DLE) has a further increased slope of the dimer fraction curve and reaches a dimerisation degree of one as the mean length reaches the saturation regime. A similar behavior is found in the model with the conventional edge diffusion mechanism (DCE). In this case the full dimerisation is reached shortly after the deposition. The curve of the model with the limited edge diffusion, however, coincides greatly with the experimental observation of very few monomer rows around one hour after the deposition. Whereas the simulation with the instantaneous diffusion implementation has a considerable lower amount of dimer particles at that time, around 65%, compared to the model with the limited variant, which has around 90% dimers at that point. The other models are even further away from that regime, the simulation without edge diffusion has a lower dimer ratio and the model with conventional edge diffusion has a far more higher ratio, respectively.

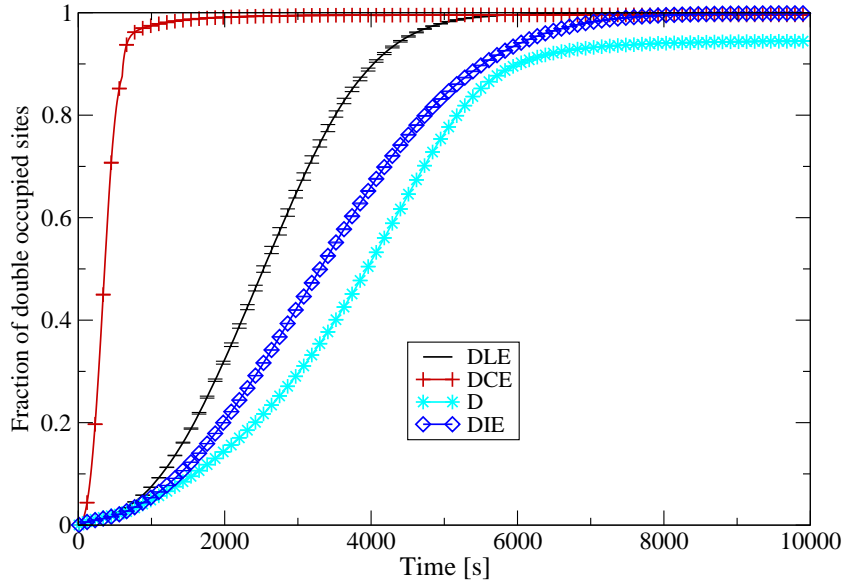


Figure 5.40: Time development of the ratio of dimer particles on the occupied sites (model IV-VII).

In figure 5.41 and 5.42 the histograms for the models with dimer structures are presented. As for the other histograms two different times are displayed. Figure 5.41 shows the histograms around one hour after the deposition and figure 5.42 the results roughly 100 minutes thereafter. In the diagram at the earlier time only the model with the conventional edge diffusion shows a peak, but at length too small compared to the experiment and additionally declines at small lengths. The size distribution for the model without edge diffusion shows no maximum and is far too shallow. In contrast the simulation with the instantaneous edge diffusion mechanism is far too broad and shows no maximum. Besides the unmatched flank at smaller sizes, the tail of the distribution for larger islands and the declining part of the peak match well for the model with edge diffusion limited by a maximum distance (DLE). At the later time displayed in figure 5.42 all simulations exhibit a peaked progression. As before the size distribution of the simulation without edge diffusion and model DCE are too shallow, the instantaneous model has the maximum at sizes too small and an excessively long tail. In contrast the model with the limited edge diffusion implementation reveals a broad peak very similar to the experiment and declines at a similar pace. Only with very small islands are discrepancies visible. The same is true for the model with the conventional edge diffusion (DCE) as shown in figures 5.34 and 5.35.

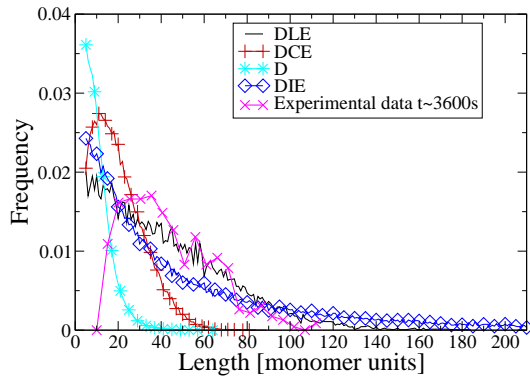


Figure 5.41: Comparison of the length histograms of the models with dimer structures and the experimental data around one hour after the deposition.

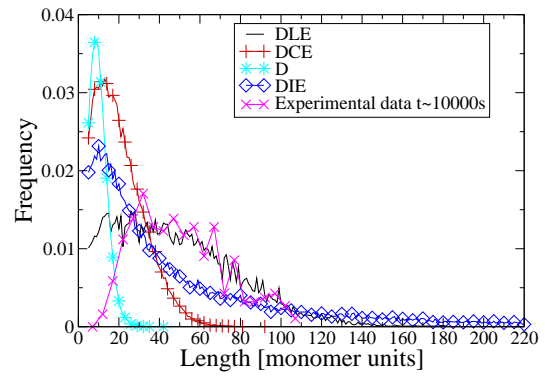


Figure 5.42: Comparison of the length histograms of the models with dimer structures and the experimental data at around 160 minutes after the deposition.

It turns out that models V (DCE) and VII (DLE) compared to all other investigated models yield a rather good description of experimental findings.

6 Summary and Outlook

In this work we have studied the ripening of one-dimensional (wire-like) helicene nanostructures on insulating (104) calcite substrates. Several models with increasing complexity have been developed and implemented in KMC simulations for explaining experimental findings. Along with these investigations we found a mechanism responsible for the observed ripening patterns.

KMC simulations reveal that in the model with one particle species and without edge diffusion the mean length grew extremely slow and the slope remained nearly unchanged during time. We found that *edge diffusion* greatly enhanced the growth of the islands during the post deposition regime in models with only monomer type particles. Even ripening and a transition to saturation could be observed in these models. Despite the similar behavior of the mean lengths, the size distributions in this case differ greatly from the experimental observed ones. The models produced rather flat distributions when ripening was exhibited (see figures 5.12 and 5.13 in Sec. 5). In addition there were high amounts of very small islands contributing to the size distribution, which disagrees further with the compact distinct peak from the experimental distributions, where the amount of small islands was very slight. Based on the model with only one particle type some valuable insights were obtained: At first ripening does occur when a certain intermediate stability of the rows exists. For smaller in-row binding energies the rows did not grow after the deposition, because of the high dissociation rates, and for larger values the dynamics were frozen and ripening was suppressed.

Thus further refinements are required. Experimental studies urged to introduce an additional *dimer* particle species. To this end dimer structures were incorporated. This way not only a new particle species was introduced but also another origin of ripening. In the model with dimer structures an enhanced growth of the mean length could be observed, even in the absence of edge diffusion (see figure 5.19). It occurred when the ratio of dimers saturated and a value of 1 (all monomer type particles are vanished) was approached. This can be understood by the fact that dimer rows are more stable than monomer rows. Therefore dimer rows can capture particles faster than they lose them due to dissociation. The cause for the observed increase of the mean length is that dimerization near dimer particles is beneficial and the more dimer particles are present the faster they accumulate. Hence when nearly all particles are dimers the small monomer rows vanish, because monomers that dissociate are more likely to find a suitable site for dimerization, and lead to the increase of the mean length.

Another special property of this model is that rows of alternating dimer and monomer species occur in a considerably amount. The absence of such rows in the models with edge diffusion is due to curing of mixed rows, because those models force edge diffusing particles on mixed rows to the first encountered site which is occupied by a different species, leading to the growth of pure dimer rows.

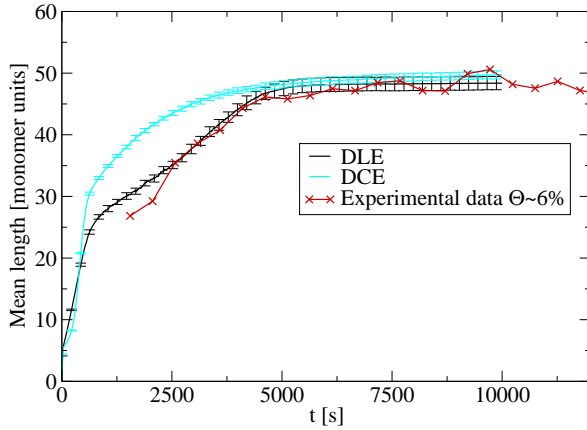


Figure 6.43: Mean length results of model V (DCE - including standard edge diffusion processes) and model VII (DLE - including edge diffusion processes limited by maximum distance) along with the experimental data.

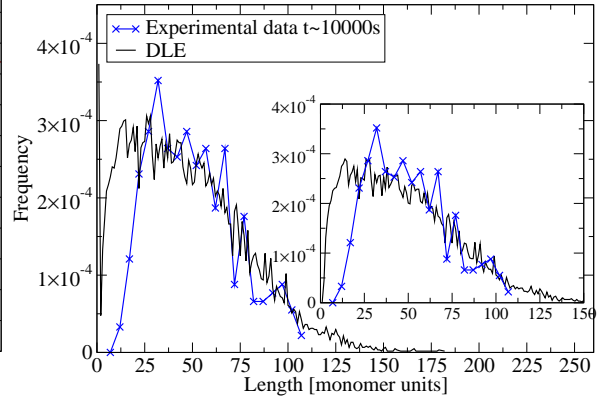


Figure 6.44: Island size distribution of model VII (DLE) with experimental data, measured 166 minutes after the deposition containing both (monomer) single rows and dimer (double) rows. The inset shows only the size distribution of double rows.

The additional implementation of dimer species was not sufficient to recreate the experimentally observed mean length progression, i.e. to introduce a regime with strong ripening right after the deposition. Hence the model including dimers was expanded with different edge diffusion mechanisms. In those models (V-VII) the existence of dimer particles and edge diffusion influence the ripening behavior. From the results of the model with instantaneous edge diffusion (VI), the inappropriateness of this implementation could be stated. It produces a very broad island size distribution with extremely large islands. This already contradicts the experimental observations. But the important dependence of the ripening on the binding energies, hence the row stability, and the intensity of the ripening was displayed very well. In contrast models V (DCE) and VII (DLE) produced mean length progressions similar to the experiment, where full dimerisation led to a saturation of the mean length, thereafter the growth of the mean length ceases or increases extremely slowly due to stochastic ripening [57]. This effect is the reason why the models which incorporated dimer structures, i.e. a species more stable than the monomers, showed a transition between enhanced ripening, where monomer structures dominated, and a saturation regime, where the enhanced stability of the dimers suppressed a further strong growth of the islands. In other words, edge diffusion processes mediate the strong ripening (regime II) and full dimerisation (single/monomer rows vanishes) leads to saturation (regime III).

To sum up, we found that results obtained with models VII (DLE), containing two species types and edge diffusion processes limited by maximum distance, and V (DCE), implementing dimer structures and conventional edge diffusion, are in excellent agreement with experimental observations (see Fig. 6.43 and 6.44).

Finally, as already mentioned during the description of the experiment in section 3.1 there are two distinct species of the helicene molecule, which differ in chirality. It would be interesting to investigate also the competition between homo- and heterochiral row types with different stabilities.

The importance of two particle species combined with edge diffusion processes is a well suited starting point for developing a mean-field rate equation approach capturing the essential features of the time-evolution of one-dimensional (wire-like) helicene nanostructures in the post-deposition regime.

7 Appendix

7.1 KMC

This section summarizes the basic ideas behind the Monte Carlo algorithm used in this thesis. First of all the basic idea for creating an approximately solution to a given stochastic process is to sample a sufficient amount of random trajectories consistent with a set of transition rates corresponding to this certain process. The properties under investigation then are not calculated via the probability densities

$$\langle Q \rangle = \frac{\sum_i Q_i e^{-\beta E_i}}{Z} \quad (7.1)$$

(with the partition function Z) but rather directly with

$$\langle Q \rangle = \frac{1}{N} \sum_i^N Q_i. \quad (7.2)$$

The prerequisite for using this formula is that the Q are sampled correctly according to the stochastic process. In many cases this is according to their Boltzmann probabilities. Thus the partition function is not needed for further calculations at all. But for using this simple relation 7.2 the simulation itself has to provide the values Q_i with the correct distribution. For designing a simulation with such a behavior the properties of Markov processes are utilized. Hence the states are not generated at random but rather generated from a previous state μ according to a set of rates that satisfy detailed balance 7.3 and therefore tending to the stationary state and thus yield samples of the correct probability distribution.

$$\rho_\mu \omega_{\mu\mu'} = \rho_{\mu'} \omega_{\mu'\mu} \quad (7.3)$$

With the transition probabilities ω and equilibrium probabilities ρ of finding the system in state μ . Furthermore the process has to fulfill the condition of ergodicity [55] which means for a simulation that every state can be reached from every other state given enough time. This is especially important because it ensures that there is always a path to the correct state (in terms of the underlying probability distribution) and the system does not become trapped inevitably in another state.

Before explaining the algorithm used in this work the easier Metropolis algorithm [58] is discussed for the well known two-dimensional Ising model to show how the properties of Markov processes are utilized for this purpose.

1. Choose a site at random
2. Calculate energy difference in case of a spin flip
3. Flip the spin if the energy difference is negative or else with probability $p = e^{-\beta\Delta E}$

This algorithm is relatively easy to implement but suffers from certain disadvantages. If the system is in a local minimum state the energy differences can become large and most moves are discarded so the dynamics freeze and a lot of computation time is wasted. The same is true for low temperatures where even small energy barriers can be associated with very low transition rates. Another problem is that this algorithm does not provide information about the dynamics of the system. With the Metropolis algorithm only information of the equilibrium state can be gathered but nothing about the evolution in time to get there. To circumvent this restrictions another Monte Carlo implementation is used here.

In this work an algorithm is used which is known under different names for example Waiting Time Monte Carlo, Continuous Time Monte Carlo or Kinetic Monte Carlo (KMC) algorithm. This algorithm was developed by Bortz, Kalos and Lebowitz and is therefore also referred as BKL algorithm. The idea behind KMC is that the system will stay in a state μ for a certain time [55]:

$$\Delta\bar{t} = -\frac{1}{\log p(\mu|\mu)} = -\frac{1}{\log(1 - \sum_{\nu \neq \mu} p(\nu|\mu))} \approx \frac{1}{\sum_{\nu \neq \mu} p(\nu|\mu)} \quad (7.4)$$

To implement this idea one has to remind the fact that processes that are conducted with a rate Γ_α have a distribution of times when the process actually takes place according to

$$\Omega(t) = \Gamma_\alpha e^{-\Gamma_\alpha t} . \quad (7.5)$$

Therefore processes with big rates have on average shorter execution times than ones with small rates. So a possible implementation consists of drawing random times with a distribution like equation 7.5 for all processes involved in the simulation and then choosing one of the possible realizations of the process with the shortest time. Then this time is used to update the global simulation time. This way it is possible to introduce a timescale in the simulation that is comparable to real experiments, consequently one can successfully simulate the kinetics of such a system. So the algorithm can be described with the following steps:

1. Calculate the rates of all possible processes
2. Draw random times with distribution 7.5 for these processes
3. Conduct the process with the shortest time
4. Update system time

Like outlined above its possible to calculate all the rates and drawing the random times at every iteration. But it is advantageous to remember the properties of a Markov process and hence only recalculate the rates that are affected from the current step. Furthermore only the times of these processes have to be redrawn because the transitions are independent of each other and so it is irrelevant if those times were drawn

before or after an independent process took place. The correct sampling of states is therefore guaranteed.

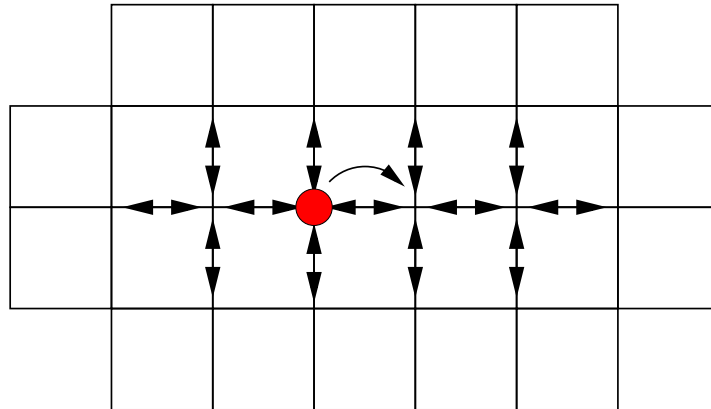


Figure 7.45: Processes, which need to be checked if there are changes after a jump in the $[010]$ direction occurred, are indicated by arrows.

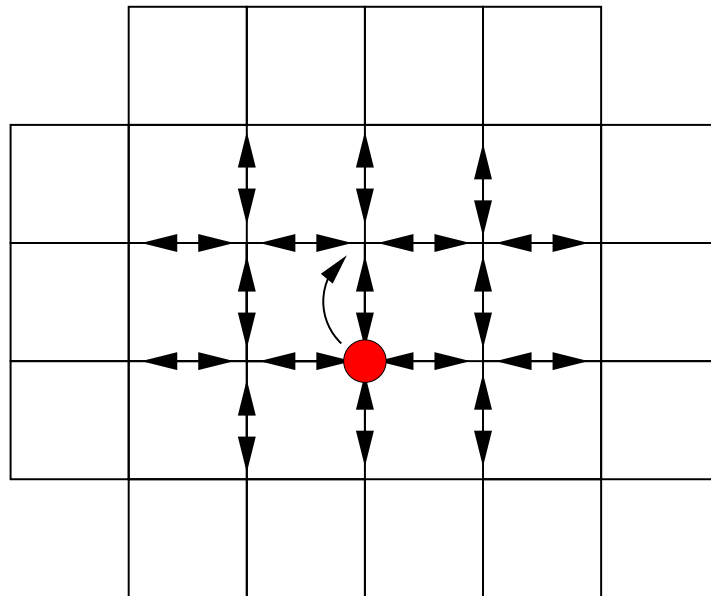


Figure 7.46: Sites are indicated by arrows that need to be checked for process updates after a jump perpendicular to the row growth direction occurred.

Some specific implementation features important for the investigation of the system covered in this thesis are given below. All processes, besides the deposition, involve a movement of one particle to an adjacent site so that the configuration for particles in the vicinity changes. This is also true after the deposition of a new particle in the vicinity of others. Hence processes around those sites need to be checked for changes in the configuration and updated accordingly after every simulation step. The affected

processes that need to be updated are different for the two possible diffusion directions and are depicted in figure 7.45 for jumps along the $[010]$ direction where neighboring particles feel an attractive force and figure 7.46 shows the affected area after a jump in the other direction.

7.2 References

- [1] Wang, N., Y. Cai and R. Q. Zhang: *Growth of Nanowires*, Material Science and Engineering, **60**, 1 (2008).
- [2] Kubatkin, S., A. Danilov, M. Hjort, J. Cornil, J. Bredas, N. Stuhr-Hansen, P. Hedegard and T. Bjornholm: *Single-electron transistor of a single organic molecule with access to several redox states*, NATURE, **425**, 698 (2003).
- [3] Aviram, A. and M. Ratner: *Molecular Rectifiers*, Chemical Physics Letters, **29**, 277 (1974).
- [4] Okawa, Y., S. K. Mandal, C. Hu, Y. Tateyama, S. Goedecker, S. Tsukamoto, T. Hasegawa, J. K. Gimzewski and M. Aono: *Chemical Wiring and Soldering toward All-Molecule Electronic Circuitry*, Journal of the American Chemical Society, **133**, 8227 (2011).
- [5] Reed, M.: *Molecular-scale electronics*, Proceedings of the IEEE, **87**, 652 (1999).
- [6] Körner, M., F. Loske, M. Einax, A. Kühnle, M. Reichling and P. Maass: *Second-Layer Induced Island Morphologies in Thin-Film Growth of Fullerenes*, Phys. Rev. Lett., **107**, 016101 (2011).
- [7] Rahe, P., M. Nimmrich, A. Greuling, J. Schütte, I. G. Stará, J. Rybáček, G. Huerta-Angeles, I. Starý, M. Rohlfing and A. Kühnle: *Toward Molecular Nanowires Self-Assembled on an Insulating Substrate: Heptahelicene-2-carboxylic acid on Calcite (1014)*, Journal of Chemical Physics, **114**, 1547 (2010).
- [8] Evans, J. W., P. A. Thiel and M. C. Bartelt: *Morphological evolution during epitaxial thin film growth: Formation of 2D islands and 3D mounds*, Surface Science Reports, **61**, 1 (2006).
- [9] Hänggi, P., P. Talkner and M. Borkovec: *Reaction-rate theory: fifty years after Kramers*, Review of Modern Physics, **62**, 251 (1990).
- [10] Michely, T. and J. Krug: *Islands Mounds and Atoms*, Springer Verlag (2002).
- [11] Brune, H.: *Microscopic view of epitaxial metal growth: nucleation and aggregation*, Surface Science Reports, **31**, 121 (1998).
- [12] Amar, J. and F. Family: *Critical Cluster-Size - Island Morphology And Size Distribution In Submonolayer Epitaxial-Growth*, Physical Review Letters, **74**, 2066 (1995).
- [13] Röder, H., K. Bromann, H. Brune and K. Kern: *Diffusion-Limited Aggregation with Active Edge Diffusion*, Physical Review Letters, **74**, 3217 (1995).
- [14] Venables, J.: *Rate Equation Approaches to Thin-Film Nucleation Kinetics*, Philosophical Magazine, **27**, 697 (1973).

- [15] Venables, J., G. Spiller and M. Hanbucken: *Nucleation and Growth of Thin-Films*, Reports On Progress In Physics, **47**, 399 (1984).
- [16] Ratsch, C. and J. A. Venables: *Nucleation theory and the early stages of thin film growth*, Journal of Vacuum Science, **21**, 96 (2003).
- [17] Walton, D.: *Nucleation of Vapor Deposits*, Journal of Chemical Physics, **37**, 2182 (1962).
- [18] Zhang, C. M., M. Bartelt, J. M. Wen, C. Jenks, J. Evans and P. Thiel: *Submonolayer island formation and the onset of multilayer growth during Ag/Ag(100) homoepitaxy*, Surface Science, **406**, 177 (1998).
- [19] Frank, S., H. Wedler, R. J. Behm, J. Rottler, P. M. K. J. Caspersen, C. R. Stoldt, P. A. Thiel and J. W. Evans: *Approaching the low-temperature limit in nucleation and two-dimensional growth of fcc(100) metal films Ag/Ag(100)*, Physical Review B, **406**, 178 (2002).
- [20] Einax, M., S. Ziehm, W. Dieterich and P. Maass: *Scaling of Island Densities in Submonolayer Growth of Binary Alloys*, Physical Review Letters, **99** (2007).
- [21] Barth, J., H. Brune, B. Fischer, J. Weckesser and K. Kern: *Dynamics of Surface Migration in the Weak Corrugation Regime*, Physical Review Letters, **84**, 1732 (2000).
- [22] Amar, J. G. and F. Family: *Kinetics of submonolayer and multilayer epitaxial growth*, Thin Solid Films, **272**, 208 (1996).
- [23] Tsui, F., J. Wellman, C. Uher and R. Clarke: *Morphology Transition and Layer-by-Layer Growth of Rh(111)*, Physical Review Letters, **76**, 3164 (1996).
- [24] Stroscio, J. A. and D. T. Pierce: *Scaling of diffusion-mediated island growth in iron-on-iron homoepitaxy*, Physical Review B, **49**, 8522 (1994).
- [25] Bartelt, M. C. and J. W. Evans: *Scaling analysis of diffusion-mediated island growth in surface adsorption processes*, Physical Review B, **46**, 12675 (1992).
- [26] Körner, M., M. Einax and P. Maass: *Island size distributions in submonolayer growth: Prediction by mean field theory with coverage dependent capture numbers*, Physical Review B, **82**, 201401 (2010).
- [27] Bales, G. S. and D. C. Chrzan: *Dynamics of irreversible island growth during submonolayer epitaxy*, Physical Review B, **50**, 6057 (1994).
- [28] Zinke-Allmang, M., L. C. Feldman and M. H. Grabow: *Clustering on surfaces*, Surface Science Reports, **16**, 377 (1992).

- [29] Ostwald, W.: *Über die vermeintliche Isomerie des roten und gelben Quecksilberoxyds und die Oberflächenspannung fester Körper*, Zeitschrift für Physikalische Chemie, **34**, 495 (1900).
- [30] Lifshitz, I. M. and V. V. Slyozov: *The Kinetics of Precipitation from Supersaturated solid Solutions*, Journal of Physics and Chemistry of Solids, **19**, 35 (1959).
- [31] Wagner, C.: *Theorie der Alterung von Niederschlägen durch Umlosen (Ostwald-Reifung)*, Zeitschrift für Elektrochemie, **65**, 581 (1961).
- [32] Chakraverty, B.: *Grain size distribution in thin films-1. Conservative systems*, Journal of Physics and Chemistry of Solids, **28**, 2401 (1967).
- [33] Haußer, F. and A. Voigt: *Ostwald ripening of two-dimensional homoepitaxial islands*, Physical Review B, **72**, 035437 (2005).
- [34] v. Smoluchowski, M.: *Three lectures on diffusion, Brown's molecular movements and the coagulation of colloid parts*, Physikalische Zeitschrift, **17**, 585 (1916).
- [35] Wen, J. M., S. L. Chang, J. W. Burnett, J. W. Evans and P. A. Thiel: *Diffusion of Large Two-Dimensional Ag Clusters on Ag(100)*, Physical Review Letters, **73**, 2591 (1994).
- [36] Lo, A. and R. Skodje: *Kinetic and Monte Carlo models of thin film coarsening: Cross over from diffusion-coalescence to Ostwald growth modes*, Journal of Chemical Physics, **112**, 1966 (2000).
- [37] Sholl, D. S. and R. T. Skodje: *Diffusion of Clusters of Atoms and Vacancies on Surfaces and the Dynamics of Diffusion-Driven Coarsening*, Physical Review Letters, **75**, 3158 (1995).
- [38] Koh, S. J. and G. Ehrlich: *Stochastic Ripening of One-Dimensional Nanostructures*, Physical Review B, **62**, R10645 (2000).
- [39] Linderoth, T. R., S. Horch, L. Petersen, E. Lægsgaard, I. Stensgaard and F. Besenbacher: *Does One-Dimensional (1D) Adatom and Cluster Diffusion of Pt on the Pt(110)-(1 × 2) Surface lead to 1D Ripening?*, New Journal of Physics, **7** (2005).
- [40] Roder, H., E. Hahn, H. Brune, J. Bucher and K. Kern: *Building one-dimensional and 2-dimensional Nanostructures by diffusion-controlled Aggregation at Surfaces*, Nature, **366**, 141 (1993).
- [41] Koh, S. J. and G. Ehrlich: *Pair- and Many-Atom Interactions in the Cohesion of Surface Clusters: Pd_x and Ir_x on W(110)*, Physical Review B, **60**, 5981 (1999).
- [42] Javorský, J., M. Setvín, I. Ošťádal and P. Sobotík: *Heterogeneous Nucleation and Adatom Detachment at One-Dimensional Growth of In on Si(100)-2 × 1*, Physical Review B, **79**, 165424 (2009).

- [43] Albao, M. A., J. W. Evans and F.-C. Chuang: *A Kinetic Monte Carlo Study on the Role of Defects and Detachment in the Formation and Growth of In Chains on Si(100)*, Journal of Physics: Condensed Matter, **21**, 405002 (2009).
- [44] Ferrando, R., F. Hontinfinde and A. C. Levi: *Morphologies in Anisotropic Cluster Growth: A Monte Carlo Study on Ag (110)*, Physical Review B, **97**, 236102 (1997).
- [45] Rybáček, J., G. Huerta-Angeles, A. Kollárovič, I. G. Stará, I. Starý, P. Rahe, M. Nimmrich and A. Kühnle: *Racemic and Optically Pure Heptahelicene-2-carboxylic Acid: Its Synthesis and Self-Assembly into Nanowire-Like Aggregates*, European Journal of Organic Chemistry, **2011**, 853 (2011).
- [46] Grunze, K.-H. E. M. N. M. and U. Ellerbeck: *NEXAFS Study on the Orientation of Chiral P-Heptahelicene on Ni(100)*, Journal of the American Chemical Society, **123**, 493 (2001).
- [47] Fasel, R., A. Cossy, K.-H. Ernst, F. Baumberger, T. Greber and J. Osterwalder: *Orientation of chiral heptahelicene C₃₀H₁₈ on copper surfaces: An x-ray photoelectron diffraction study*, Journal of Chemical Physics, **115**, 1020 (2001).
- [48] Ernst, K.-H., Y. Kuster, R. Fasel, M. Muller and U. Ellerbeck: *Two-Dimensional Separation of [7]Helicene Enantiomers on Cu(111)*, Chirality, **13**, 675 (2001).
- [49] Lee, T. D. and C. N. Yang: *Statistical Theory of Equations of State and Phase Transitions. II Lattice Gas and Ising Model*, Physical Review, **87**, 410 (1952).
- [50] Jacobson, J. D., W. Fickett and W. W. Wood: *Application of the Monte Carlo Method to the Lattice-Gas Model. I. Two-Dimensional Triangular Lattice*, Journal of Chemical Physics, **30**, 65 (1959).
- [51] Evans, J. W., D. E. Sanders, P. A. Thiel and A. E. DePristo: *Low-temperature epitaxial growth of thin metal films*, Physical Review B, **41**, 5410 (1990).
- [52] Sanders, D. E., D. M. Halstead and A. E. DePristo: *Metal/metal Homoepitaxy on fcc(111) and fcc(001) Surfaces: Deposition and Scattering from small Islands*, Journal of Vacuum Science and Technology, **10**, 1986 (1992).
- [53] Gomer, R.: *Diffusion of adsorbates on metal surfaces*, Reports on Progress in Physics, **53**, 917 (1990).
- [54] Kellogg, G. L.: *Field ion microscope studies of single-atom surface diffusion and cluster nucleation on metal surfaces*, Surface Science Reports, **21**, 1 (1994).
- [55] Newman, M. and G. Berkema: *Monte Carlo Methods in Statistical Physics*, Clarendon Press (1999).
- [56] Weckesser, J., J. V. Barth and K. Kern: *Direct Observation of Surface Diffusion of Large Organic Molecules at Metal Surfaces: PVBA on Pd(110)*, Journal of Chemical Physics, **110**, 5351 (1999).

- [57] Ludwig, F. P., J. Schmelzer and J. Bartels: *Influence of Stochastic Effects on Ostwald Ripening*, Journal of Material Science, **29**, 4852 (1994).
- [58] Metropolis, N., A. Rosenbluth, M. Rosenbluth, A. Teller and E. Teller: *Equation of State Calculations by Fast Computing Machines*, Journal of Chemical Physics, **21**, 1087 (1953).

7.3 Erklärung

Hiermit erkläre ich, dass ich diese Arbeit selbstständig durchgeführt und abgefasst habe. Quellen, Literatur und Hilfsmittel, die von mir benutzt wurden, sind als solche gekennzeichnet.

7.4 Acknowledgements

At this point I want express my gratitude to all who assisted and supported me during the work on this thesis.

First I would like to thank Mario Einax for supervising and mentoring this work and his continuing support. I also want to thank Philipp Maaß, who agreed to be a referee for this thesis.

Furthermore I want to express my gratitude to Martin Körner for providing the basis code for the computer simulation, as well as for the support and helpful discussions concerning technical details and the underlying physics.

Next, I want to thank the group of Angelika Kühnle at the University of Mainz for making their measurement data concerning the helicene experiment available and hence providing the inspiration for this thesis.

I am very grateful to Steve and Claudia Lenk, Adam Williamson, Christian Trott, David Leipold, Markus Reinmöller and Thomas Hänsel as well as to all the other colleagues in the department of physics, especially the two departments for theoretical physics, for the pleasant working atmosphere.

Last but not least I want to show my gratitude to my friends, my fellow students, and my family for the ongoing support and help.